REVISION 2

Mineralogical evolution of Fe−Si-rich layers at the olivine-water interface during carbonation reactions

Giuseppe D. Saldi[1,*,⊥], Damien Daval[2,⊥], Hua Guo[1], François Guyot[3], Sylvain Bernard[3], Corentin Le Guillou[3], James A. Davis[1], and Kevin G. Knauss[1]

[1]*Earth Sciences Division, Lawrence Berkeley National Laboratory, 1 Cyclotron Road, Berkeley, CA 94720, USA.*
[2] *Laboratoire d'Hydrologie et de Géochimie de Strasbourg, Université de Strasbourg/EOST-CNRS UMR 7517, 1 Rue Blessig, 67084 Strasbourg, France*
[3]*Institut de Minéralogie, de Physique des Matériaux et de Cosmochimie, IMPMC, Sorbonne Universités, CNRS UMR 7590, MNHN, UPMC, IRD UMR 206, 61 rue Buffon, 75005 Paris, France*

[*]Corresponding author. Present address: *GET, CNRS/UMR 5563-Université Paul Sabatier, 14 ave. E. Belin, 31400 Toulouse, France.*
Phone: +33 (0)5 6133 2649
E-mail address: giuseppe.saldi@get.obs-mip.fr (G.D. Saldi)
[⊥] Equal contribution from the first two authors.

Abstract

Recent studies investigating carbonation of iron-bearing silicates have shown that the rates of these reactions, although formally not depending on oxygen fugacity, are strongly different at different redox states of the system (Saldi et al. 2013; Sissmann et al. 2013). Here we provide a micro- and nanostructural characterization of the olivine/water interface during the carbonation of forsteritic olivine at 150 °C and pCO_2 = 100 bar. When the reaction starts under oxic conditions, the observed temporal sequence of interfacial layers consists of: a hematite/$SiO_{2(am)}$ assemblage, Fe-rich phyllosilicates with mixed Fe valence and a non-passivating Fe-free amorphous SiO_2 layer, which allows the formation of ferroan magnesite. In contrast, starting at micro-oxic conditions, carbonation rates are much faster, with no real evidence of interfacial layers. Separate deposits of goethite/lepidocrocite in the early stages of the reaction and then formation of magnetite are observed at these conditions, while precipitation of siderite/magnesite proceeds unhindered. The evolution of the redox conditions during the reaction progress controls the sequence of the observed reaction products and the passivating properties of Fe–Si-rich interfacial layers. These findings have important implications for modeling the carbonation of ultramafic rocks under different oxygen fugacity conditions as well as for understanding the technological implications of adding accessory gases to CO_2 in carbon capture and storage mineralization processes involving ultrabasic rocks.

Keywords: olivine carbonation, Fe–Si-rich interfacial layers, redox reactions, passivation, cronstedtite, dissolution/precipitation, Fe-oxides.

INTRODUCTION

The formation of amorphous Si-rich layers and other secondary precipitates at the mineral/water interface is a well-known process that takes place during the chemical weathering of silicate minerals and can have a significant impact on their dissolution behavior (e.g., Velbel et al. 1993; White and Brantley 2003; Schott et al. 2012; Daval et al. 2013). Irrespective of the exact mechanism of their formation, it is acknowledged that Si-rich altered layers form independently of the degree of saturation of the bulk solution with respect to pure silica polymorphs (cf. Casey et al. 1993; Hellmann et al. 2012). The elementary processes that control the formation and properties of silica altered layers are complex and depend on a series of different factors, such as the structure and composition of the parent phase, the incorporation of foreign ions and the degree of hydration of the silica layers, which may decrease their solubility with respect to pure silica phases (cf. Iler 1979; Schott and Berner 1983; Daval et al. 2009; Hellmann et al. 2012; Daval et al. 2013). Because the development of Si-rich surface layers variably inhibits the dissolution reaction, their formation can also affect significantly a wide range of environmental and/or engineering processes, such as geological CO_2 sequestration, since the rate of CO_2 consumption and the extent of coupled carbonation reactions rely upon the availability of divalent cations released by the dissolution of primary silicates (cf. Oelkers et al. 2008; Guyot et al. 2011). Olivine [$(Mg,Fe)_2SiO_4$] is one of the most thermodynamically favorable and fastest dissolving phases (cf. Oelkers 2001; Schott et al. 2009) and for this reason, it has been the object of a relevant number of studies focusing on the elementary processes and the conditions that enhance, or limit, the overall carbonation reaction (Giammar et al. 2005; Andreani et al. 2009; Garcia et al. 2010; Gerdemann et al. 2007; Dufaud et al. 2009; King et al. 2010; Qafoku et al. 2012; Wang and Giammar 2012; Saldi et al. 2013; Sissmann et al. 2013;

Johnson et al. 2014). The formation of Si-rich layers exhibiting some passivating properties on the olivine surface was investigated by several authors (e.g., Béarat et al. 2006; Davis et al. 2009; Daval et al. 2011), whose results suggest that the protective action and evolution of amorphous SiO_2 layers do vary as a function of temperature and with the chemical compositions of the aqueous fluid. For instance, Daval et al. (2011) showed that, at 90 ºC, in a CO_2-saturated pure H_2O system, the olivine surface is affected by the formation of a thin and uniform amorphous layer that is stabilized as the bulk aqueous solution approaches the saturation with respect to amorphous SiO_2 and is responsible for the dramatic decrease of mineral reactivity. Eventually, the development of an impermeable coating can prevent the aqueous fluid from reaching the saturation with respect to Mg-carbonates, thus inhibiting the carbonation reaction. On the other hand, Béarat et al. (2006), who conducted some experiments at 185 ºC, at high ionic strength and under high concentrations of $NaHCO_3$, reported a more porous structure of the Si-rich coating, which favored the intergrowth of magnesite crystals, leading to high extents of carbonation. These authors also observed the recurring cracking and exfoliation of the passivating layer, a process that was explained with the rapid polymerization of silanol groups to form a more condensed structure (see also Olsson et al. 2012).

In a previous study (Saldi et al. 2013), we pointed out the fundamental role of Fe^{3+}/ Si interaction in controlling the passivating properties of precipitated Si-rich coatings. We suggested that the evolution of the redox conditions during the course of the reaction affects the nature of the secondary phases formed at the fluid/solid interface and thus the rate of the overall reaction. Sissmann et al. (2013) reported similar observations and showed that the formation of passivating layers can be inhibited by the addition of organic ligands such as citrate. This

suggests that the complexation of Fe in solution could retard or impede its incorporation within the SiO_2-rich layer, thus preventing its passivating effect.

Despite the lack of any direct evidence of the physico-chemical microstructure of the Fe−Si-rich interfacial layer, Saldi et al. (2013) presented a qualitative model to describe the chemical transformation of the olivine/water interface at 150 °C, which postulated the formation of a primitive Fe-rich amorphous SiO_2 layer and its successive breakdown in favor of a more stable mixed Fe(II)-Fe(III) phase as conditions became progressively anoxic.

Here we report the micro- to nano-scale characterization of the olivine/water interface submitted to similar experimental conditions (pCO_2=100 bar, T=150 ºC). The direct study of the mineral surface and its physico-chemical evolution as a function time was accomplished by the combination of advanced microscopic and spectroscopy techniques (focused ion beam (FIB) milling - transmission electron microscopy (TEM) and scanning transmission X-ray microscopy (STXM)). This approach allowed us to document fine-scale mineralogical transformations and provide new insights to better constrain the elementary processes that underline the model of Saldi et al. (2013).

MATERIALS AND EXPERIMENTAL METHODS

Starting materials and experimental setup

A detailed description of the starting materials and the experimental setup can be found in Saldi et al. (2013). Ultrasonically cleaned olivine crystals (Fo_{88}) from San Carlos (Arizona, USA) with 149–295 μm grain size and specific surface area of 0.015 m^2/g (measured by Kr adsorption analysis using the BET method) were used to perform carbonation experiments at 150 °C and pCO_2= 100 bar. Batch experiments were conducted in flexible Au bag hydrothermal

system (Seyfried et al. 1979; Knauss and Copenhaver 1995), in which fluids are in contact with pure Au and commercially pure Ti. Before use, the Ti-parts were first acid-cleaned in hot nitric acid for about 30 minutes and then passivated overnight at 450 °C. Pressure was controlled using a high pressure syringe pump (Teledyne Isco 500 D) injecting deionized water into the pressure vessel, outside of the Au bag, contained in a large tube furnace. Injection of liquid CO_2 at 100 bar pressure was achieved by using a second high pressure syringe pump. The furnaces were continuously rotated at 180°/min throughout the experimental runs. The aqueous fluid was sampled from the Au bag by turning the autoclaves upside-down. In this way, supercritical CO_2 migrated upward, while the fluid could be retrieved at the opposite side of the cell via the high pressure sampling valve, avoiding any possible decrease of CO_2 pressure inside the Au-cell. The aqueous samples were filtered using an internal 10 μm Ti frit and a 0.22 μm Millipore filter, prior to acidification using ultrapure concentrated (68%) nitric acid. The 31-day experiment (run Ol-150) described in Saldi et al. (2013) is here renamed Ol-150-1d. Three additional experiments were conducted under the same conditions, using deionized water equilibrated with the atmosphere, and were stopped after time durations of 7, 17 and 19 days (runs Ol-150-1a-c) to recover solid samples before, at, and after the change from oxic to anoxic conditions revealed by the sudden release of Fe into the fluid (see below).

A supplementary batch experiment was conducted under low O_2 fugacity conditions (Ol-150-2) to further assess the influence of redox conditions on the mineralogical nature of the interfacial layers. Before assembling the reaction cell, distilled deionized (DDI) water was purged with a constant flow of methane at 1 bar pressure for about 60 minutes. The fluid was then immediately poured in the Au-cell containing 2 g of solid material and the system was sealed with a Ti-head closure, while keeping the headspace of the cell pressurized with 1 bar of

CH_4 to maintain the system under low oxygen fugacity (fO_2). Before injecting liquid CO_2 into the system, 20 ml of CH_4 at a pressure of 7 bars were added to the reaction cell, after having leak-tested the entire assembly (Au-cell + pressure vessel) overnight. Although this procedure could not make the aqueous medium completely anoxic (see discussion below), it was sufficient to decrease significantly the $O_{2(aq)}$ concentration compared to the set of experiments conducted with a fluid equilibrated with the atmosphere. As a consequence, we will refer to those conditions as "micro-oxic", to distinguish them from the oxic conditions of the other experiments. A comprehensive summary of the experiments conducted in this study is reported in Table 1.

Aqueous solution analyses, thermodynamic calculations and total carbon (TC) measurements

All collected fluid samples were analyzed for Mg, Fe and Si by Inductively Coupled Plasma – Optical Emission Spectroscopy, ICP-OES (Varian 720 ES). All speciation and solubility calculations were executed using the geochemical code PHREEQC v. 2.17 (Parkhurst and Appelo 1999) using its LLNL thermodynamic database. Activity coefficients for dissolved species were calculated using the Debye–Hückel equation, whereas the fugacity coefficient for CO_2 was computed using the software ThermoSolver 1.0 (Barnes and Koretsky 2004; Barnes 2006). The aqueous Mg, Fe and Si concentrations served as input to PHREEQC for computing the in situ pH and saturation indices with respect to the solid phases of interest at the calculated CO_2 fugacity (fCO_2= 85 bar).

Measurements of total inorganic carbon concentration were conducted on the powders retrieved after all the experiments. The total carbon content (TC %) was measured by catalytic oxidation at 900 °C using a non-dispersive infrared detector (TOC analyzer Shimadzu SSM

158 5000A). The TC values were used to calculate the relative extents of carbonation [EC(%)]
159 following Saldi et al. (2013), which express the percentages of initial olivine that were converted
160 to magnesite during the course of the reaction. Apart from experiment Ol-150-1d, for which the
161 TC value was reported by Saldi et al. (2013), the only powder containing measurable amounts of
162 solid carbon was the one retrieved after the run Ol-150-2. For all characterizations, we neglected
163 any possible formation of organic carbon by assuming that the measured TC is entirely
164 representative of the precipitated magnesite crystals. The large uncertainty associated with the
165 corresponding EC(%) results from the heterogeneous distribution of carbonate products within
166 the reacted solid, which may form separate crystals and lamellar aggregates in combination with
167 $SiO_{2(am)}$.

168 **Electron microscopy and focused ion beam (FIB) milling**

169 Samples of reacted powders were mounted on adhesive carbon tabs, covered with a
170 Au/Pd coating and analyzed by scanning electron microscopy (SEM) (Zeiss EVO MA10) to get
171 an overview of the dissolved olivine grains and secondary phases at the μm-scale.

172 For further nanoscale characterization, ultrathin electron-transparent cross-sections were
173 cut from selected locations on various samples using a focused ion beam (FIB) of type FEI
174 Helios 600 Nanolab dual-beam (CP2M, Marseille, France) or a FEI Strata 235 dual-beam
175 (LBNL, Berkeley, USA). The FIB Ga ion milling was carried out at an ion beam voltage of 30
176 kV and with beam currents from 3 nA to 10 pA for the final steps. Micrometer-thick sections
177 were *in situ* lifted out using an Omniprobe 200 micromanipulator and transferred to a Cu half
178 copper grid for final ion milling to electron transparency (final thickness of about 100 nm). Of
179 note, this procedure maintains textural integrity, even in the case of loosely consolidated
180 materials (Langford 2006; Drobne et al. 2007), and prevents shrinkage and deformation of

181 microscale to nanoscale pores, even in the case of highly sensitive materials (e.g., Smith et al.
182 2001; Thompson et al. 2006). Milling at relatively low Ga-ion currents at the final stages of
183 sample preparation minimizes common artifacts like local gallium implantation, mixing of
184 components, creation of vacancies or interstices, creation of amorphous layers, local
185 compositional changes or redeposition of the sputtered material on the sample surface (Rubanov
186 and Munroe 2004; Mayer et al. 2007).

187 Transmission electron microscopy (TEM) observations were performed on FIB foils using
188 a JEOL 2100 (LaB6) TEM (200 kV) or a JEOL 3010 (300 kV). Electron dispersive X-ray (EDX)
189 spectra were acquired to probe the chemical compositions, with a focused electron beam (1 nm).
190 Selected area electron diffraction (SAED) patterns were obtained to identify the observed
191 mineral phases based on their electronic diffraction patterns.

192 **Scanning Transmission X-ray Microscopy (STXM)**

193 Scanning Transmission X-ray Microscopy (STXM) is a synchrotron-based
194 spectromicroscopy technique which was used here to measure the redox of iron in the secondary
195 phases. In addition to imaging at the 15-nm scale, this technique allows collecting X-ray
196 absorption near edge structure (XANES) spectra. XANES spectra were collected for the present
197 study at the Fe-$L_{2,3}$ edge to provide information about iron valence. A spectral resolution of 0.15
198 eV was chosen for the key energy ranges, i.e., between 705 and 712 eV and between 718 and
199 725 eV. For our investigation, STXM measurements were done using the beamline 10ID-1
200 located at the Canadian Light Source (CLS, SM beamline - Kaznatcheev et al. 2007). This
201 beamline uses soft X-rays (130-2500 eV) generated with an elliptically polarized undulator
202 (EPU) inserted in the 2.9 GeV synchrotron storage ring (250-100 mA). The microscope chamber
203 was evacuated to 100 mTorr after sample insertion and back-filled with He. Dwell time was one

204 millisecond per pixel. The absorption images of the stack were aligned using the automated
205 image alignment routine of the aXis2000 software (ver2.1n - available at
206 http://unicorn.mcmaster.ca/aXis2000.html), which was also used to extract XANES spectra from
207 image stack measurements. Peaks positions and intensities were determined using the Athena
208 software package (Ravel and Newville 2005). Quantification of the $Fe^{3+}/\sum Fe$ ratio was obtained
209 using calibrations established on standards of known compositions (Bourdelle et al. 2013; Le
210 Guillou et al. 2015).
211

212 # RESULTS

213 ## Fluid chemistry evolution as a function of O_2 levels:

214 ### a. starting under oxic conditions

215 Four experiments were carried out at T =150 °C and fCO_2=85 bar for different durations (7, 17,
216 19 and 31 days). The changes of Mg and Si concentrations in the fluid (Fig. 1, Table 2) during
217 the first 6 days of reaction substantially reflect the slightly non-stoichiometric dissolution of
218 olivine, the aqueous [Mg]/[Si] ratio being higher (>1.80) than the corresponding ratio in the solid
219 (1.76). However, after this time interval, Mg concentration constantly decreased until the end of
220 the 31-day experiment due to the nucleation and growth of magnesite. The EC(%) calculated
221 from the measured TC content was equal to 15% for this experiment (Saldi et al. 2013), but we
222 could not provide any estimate for the EC(%) of the three shorter duration runs because the TC
223 levels in the reacted powders were below the detection limit. We observed an almost linear
224 increase of Si concentration from day 1.7 to day 19, while Fe remains undetectable (Fig.1a-c).
225 Experiment Ol-150-1d (Fig. 1d) shows that Fe dissolved only after 20 days, concomitantly with a
226 sudden increase of Si concentration. Based on the cumulative aqueous Mg and Si concentrations,

the calculated dissolution rates normalized to the corresponding duration of the considered run are 3.4×10^{-10}; 1.68×10^{-10}; 1.63×10^{-10}; 1.89×10^{-10} mol/cm^2/min after 7; 17; 19 and 31 days, illustrating that olivine dissolution ultimately resumed after a relative decline of the dissolution rate. The similarities in fluid chemical data for the four experiments (O-l50a-d) pinpoint specific reaction mechanisms controlling the evolution of the mineral/water interface.

b. starting under micro-oxic conditions

Results of the 1-month long experiment conducted at initially low-O_2 concentration (Ol-150-2, Fig. 2, Table 3) are very different from the run performed under initial oxic conditions (Ol-150-1a-d). Fe was rapidly dissolved and became measurable after only one hour of experiment (T=150 °C, fCO$_2$=85 bar), while Si concentration exceeded the amorphous silica saturation after 2 days (keeping the aqueous solution supersaturated for the rest of the experiment) and Mg concentration reached a maximum at the first day and then monotonically decreased until the end of the experiment. Olivine dissolution thus appears to proceed faster than in the initially oxic conditions (Ol-150-1a-d). The rapid decrease of the aqueous [Mg]/[Si] ratio to values lower than unity indicates a fast dissolution rate and the early formation of Mg-bearing secondary phases. TC values further support this evidence, showing on average an EC(%) of 57±17 %, which is about 4 times higher than the corresponding carbonation yield obtained in the initially oxic experiment (EC(%) of Ol-150-1d was 15%). Based on the averaged EC% value, the percentage of olivine consumed during this run was estimated to reach 61 % against the 19% obtained for the corresponding experiment carried out under initially oxic conditions (cf. Saldi et al. 2013).

The measured aqueous [Fe]/[Si] ratio was largely lower than the olivine stoichiometric value (Fe/Si = 0.24), as shown in Table 3. These values are consistent with the formation of both Fe-oxides and (Mg, Fe)-carbonate solid solutions.

Mineralogical, chemical and structural characterization of the olivine/fluid interface by SEM, TEM and STXM:

a. Evolution of the interface in initially oxic conditions experiments (Ol-150-1)

SEM observations allowed documenting the olivine surface evolution as a function of the reaction progress. A heterogeneous and non-uniform layer can be observed at the surface of olivine grains after 7, 17 and 19 days, before the sharp release of Fe (Fig. 3a-c). EDX spot analyses reveal a few percent increase of Fe on the coated portions of the olivine grains (typically 8-13 % by weight) compared to the uncoated areas, indicating the incipient precipitation of Fe-rich phases during the first stage of dissolution (see below). In contrast, after 31 days of experiment, olivine grains appear extensively covered by a thick coating of carbonates and a layer characterized by the presence of $SiO_{2(am)}$ spherules (Fig. 3d). It has to be noted that the occurrence of magnesite crystals, with a diameter of up to 10 μm, was also observed in the solids reacted for 17 and 19 days (runs Ol-150-1b and Ol-150-1c, respectively). These crystals were mostly found not associated with the reacted olivine surface (not shown), but there is occasional evidence for their formation in contact with the olivine grains (Fig. 3b).

TEM observations show that the mineral interface of the 7-day run is characterized by a layer of variable thickness (0.5 to 3 μm), with a heterogeneous structure (Fig.4). It is mostly composed of aggregates of acicular hematite particles and amorphous silica, as indicated by the indexing of SAED patterns (Fig. 4b) and by EDX spot analyses (spectra of Fig. 4c and 4d). In

general, the contact between the pristine olivine surface and the Fe-Si-rich layer is sharp, without any evidence of concentration gradients between the unexposed mineral and the altered layer. Along some sections, particularly in etch pits (Fig.4c), the aggregates appear loosely attached to the olivine surface, while the same material may form a thinner and denser structure in close contact with the mineral in some other areas (Fig. 4d). However, no significant compositional variations are observed among the different analyzed areas of the interfacial layer (EDX spectra of Fig.4c and 4d).

The interface of the 17-day run (Ol-150-1b) exhibits an evident change in the properties of the materials compared to the first 7 days of reaction. This is concomitant with (and likely related to) what we refer to as the 'oxic/anoxic transition', which occurred just before the sharp release of Fe to the aqueous solution (Fig.1d). In addition to an inner layer (~ 50 nm-thick) comparable to the one observed after 7 days, i.e., in contact with the olivine surface and mostly consisting of an evolved assemblage of $SiO_{2(am)}$ and Fe-oxides (Fig. 5a, spot 2), TEM reveals the presence of an outer layer primarily composed of Fe-rich phyllosilicates (Fig. 5a, spot 1). Both indexing of SAED patterns (Fig. 5b) and measurements of the inter-reticular spacing on HRTEM images (Fig. 5d) indicate that the structure of this Fe-phyllosilicate is compatible with that of cronstedtite, a mixed Fe(II)-Fe(III) phyllosilicate, whose general formula can be written as (cf. Hybler et al. 2000): $(Fe^{2+}_{3-X}Fe^{3+}_{X})[Si_{2-X}\ Fe^{3+}_{X}O_5](OH)_4$, where $0<X<1$. The corresponding EDX analyses performed on single crystal aggregates are also consistent with this formula, showing a Fe/Si ratio varying between 1.4 and 3.3. In agreement with this suggestion, STXM analyses show that the Fe-phyllosilicate is composed of both ferrous and ferric iron (Fig. 6). Nonetheless, the $Fe^{3+}/\sum Fe$ ratio determined from the peak area ratios at the Fe^{3+} $L_{2,3}$-edges of the XANES spectra (L_2-L_3 average value), based on established calibrations (cf. Bourdelle et al. 2013; Le

Guillou et al. 2015), leads to values of 83±3 % for the Fe-phyllosilicate. This Fe^{3+} content is too high with respect to the cronstedtite general formula reported in different publications (e.g., Geiger et al. 1983; Smrčok et al. 1994; Hybler et al. 2000) but is consistent with the formation of Fe^{3+}-rich serpentine minerals of variable Fe^{3+} content (cf. Evans 2008; Andreani et al. 2013). Taken together, the results from both TEM and STXM investigations point out that the identity of this Fe-phyllosilicate assemblage may be neither unique, nor unequivocal. Arguably, the assemblage of Fe-phyllosilicates observed in this sample may represent a precursor of a mineral with a univocal identity, for which cronstedtite is a likely candidate. For these reasons we will refer to this Fe-phyllosilicate as a 'cronstedtite-like' phase.

As in the 7-day run, the interfacial layer may exhibit either a relatively compact structure, with irregularly stacked and aggregated particles (Fig. 5a), or a loose and porous structure containing individual aggregates characterized by concentric structures of 50-100 nm in diameter (Fig.5c).

Additional mineralogical changes occur in the final stage of the carbonation reaction (between 17 and 31 days), as illustrated by observations on samples from the experiment Ol-150-1d. Olivine grains are uniformly covered by agglomerates of magnesite crystals of variable thickness (0.5-2.5 μm) with the interposition of an altered layer (Fig. 7a), mostly composed of amorphous silica (Fig. 7b) with remnants of hematite crystals. No clear trace of residual Fe-silicate crystals could be observed.

b. Fe-oxides formed under initially micro-oxic conditions (Ol-150-2)

The thick carbonate layer formed on top of the olivine surface after 31 days of reaction and the extensive consumption of the olivine powder by dissolution under anoxic conditions (Fig. 8) prevented the extraction of a FIB foil from the interface between the carbonate and the pristine

317 olivine. SEM investigations do not bring any particular evidence of the formation of a thick Fe-
318 Si-rich altered layer at the olivine/water interface (Fig. 8a-b), but only show the presence of
319 amorphous silica particles, mostly in contact with the uncovered olivine surface (not shown), as
320 well as SiO_2-free micrometric aggregates of Fe-oxides among the carbonated olivine grains.
321 These aggregates are found as several single grains, separately from the olivine surface and from
322 any other reaction product, and are composed of a compact mass of sub-micrometric, ellipsoidal
323 particles, overlain by micrometric Fe-oxide crystals displaying the typical octahedral habit of
324 magnetite (Fig. 9) (Cornell and Schwertmann 2003; Hu et al. 2010). The Fe-oxide particles
325 exhibit three main morphologies, as indicated by TEM analyses performed on FIB foils (Fig.
326 10). Small rounded particles, with a diameter between 20 and 90 nm, were identified as goethite
327 by indexing of SAED patterns and are found irregularly dispersed in the inner part of the
328 aggregate. These particles are in contact with vertically elongated crystals displaying a width of
329 0.2-0.4 μm and an average length of about 0.7 μm (Fig. 10), which were identified as
330 lepidocrocite according to the SAED pattern. These phases form the substratum of the bigger
331 sub-octahedral to octahedral crystals observed by SEM, which were identified as magnetite after
332 indexing of the corresponding SAED pattern (Fig10).
333

334 ## DISCUSSION

335 In agreement with the predictions of Sissmann et al. (2013) and Saldi et al. (2013), we
336 evidence here a change in the passivating effect of the interface layer resulting from the
337 evolution of the redox state of the system during the carbonation reaction. To account for their
338 macroscopic observations, both studies suggested a similar scenario for initially oxic conditions,
339 namely: (i) the early formation of a passivating Fe(III)-Si-rich phase/assemblage, progressively

consuming the aqueous O_2; (ii) the replacement of this material by a mixed Fe(II)-Fe(III) phase when the conditions become anoxic. Such replacement would be at the origin of the change of physical properties of the interfacial layer and the consequent increase of olivine dissolution. The present study reports the formation of a cronstedtite-like Fe(II)-Fe(III) phyllosilicate at the expense of the initial Fe−Si-rich protective coating, prior to the observed resumption of olivine dissolution, thus showing a substantial agreement between the experimental observations and the proposed reaction model.

The nm-scale characterizations of the alteration layer show that the initial oxygen level of the reacting fluid controls the nature of the alteration products and influences the subsequent evolution of the mineral/fluid interface, which ultimately affects the extent of the overall carbonation reactions.

In the next subsections we discuss the results of the analytical work, describe the elementary reactions involved in the formation of the observed mineral phases and provide some hints on the elementary mechanisms that control nature and properties of the Fe−Si-rich surface layers as a function of the dissolved O_2 concentration.

Reaction sequence in the initially oxic scenario:

Under initially oxic conditions, the mineralogical evolution of the Fe–Si-rich layer can be schematically summarized by a sequence of reactions characterizing the three different stages of olivine carbonation. In the first stage of the overall reaction, the Fe^{2+} released by olivine dissolution is rapidly oxidized to Fe^{3+} and precipitates as hematite (Fe_2O_3) according to:

$$Mg_{1.8}Fe_{0.2}SiO_4 + 4CO_2 + 4H_2O \rightarrow 1.8\ Mg^{2+} + 0.2\ Fe^{2+} + 4HCO_3^- + H_4SiO_4^0 \quad (1)$$

$$4Fe^{2+} + O_{2(aq)} + 4H_2O \rightarrow 2Fe_2O_3 + 8H^+ . \quad (2)$$

362 During and following hematite formation, aqueous SiO_2 is adsorbed at the surface of
363 hematite nanocrystals. This sorption reaction can be described by:

364 $$\equiv FeOH^0 + Si(OH)_4^0 \rightarrow \equiv FeH_2SiO_3^{\square} + H^+ + H_2O\ , \quad (3a)$$

365 $$\equiv FeOH^0 + Si(OH)_4^0 \rightarrow \equiv FeH_3SiO_4^0 + H_2O\ , \quad (3b)$$

366 where $\equiv FeOH^0$ represents the hematite surface hydroxyl groups (cf. Dzombak and Morel 1990)
367 and $\equiv FeH_2SiO_4^-$ and $\equiv FeH_3SiO_4^0$ denote the Fe-Si surface species forming by adsorption of
368 silicic acid on hematite, with reaction (3b) likely dominating over (3a) with increasing Si
369 concentrations (cf. Davis et al. 2002; Rusch et al. 2010). The strong Fe-Si interactions may have
370 favored the nucleation and growth of $SiO_{2(am)}$ associated with hematite, as observed by TEM
371 (e.g., Fig. 4c-d).

372 This (hematite + $SiO_{2(am)}$) assemblage corresponds to the layer which exerted the observed
373 inhibiting action on dissolution during the first 7 days of reaction. On the basis of the cumulative
374 Mg and Si aqueous concentrations, ~1.0 mmol of olivine was dissolved after 7 days. If we take
375 into account the stoichiometry of reactions (2) and (3) and consider that the initial $O_{2(aq)}$
376 concentration is fixed by the equilibrium with the atmosphere ($[O_{2(aq)}] = 0.26$ mmol/l) , nearly all
377 $O_{2(aq)}$ was consumed at the end of the experiment Ol-150-1a, leading to an anoxic medium. At
378 this stage we can calculate that approximately 0.045 mmol of hematite formed.

379 In the second stage of the process (7-17 days), the Fe–Si-rich layer underwent a
380 mineralogical transformation, with the replacement of Fe_2O_3 and associated SiO_2 by Fe(II)-
381 Fe(III)-phyllosilicates (Fig. 5), which are likely precursors of cronstedtite (see above). The
382 formation of these Fe-silicates is driven by the stabilization of Fe^{2+} in solution, which is the
383 consequence of the 'oxic-to-anoxic' transition, and can be described by:

384 $$Fe_2O_3 + SiO_{2(am)} + 2Fe^{2+} + 4H_2O \rightarrow (Fe^{2+}_2\ Fe^{3+})[Si\ Fe^{3+}]O_5(OH)_4 + 4H^+, \quad (4)$$

where the Fe-phyllosilicate in reaction (4) is represented by the formula of the Fe^{3+}-rich cronstedtite endmember, for sake of simplicity. The formation of this phase from the (hematite + $SiO_{2(am)}$) assemblage brings about the consumption of all the $SiO_{2(am)}$ associated with the ferric-oxide. We also suggest that, via reaction (4), hematite is reduced by the catalytic action of the Fe^{2+} ions released by olivine dissolution, which implies an electron transfer from adsorbed Fe(II) to structural Fe(III) of hematite (Williams and Scherer 2004). Such reaction mechanism drives most of the inter-conversion reactions between Fe-oxides (e.g., Jeon et al. 2003; Pedersen et al. 2005; Jones et al. 2009) and may explain the rapid formation of the observed Fe(II)-Fe(III)-phyllosilicate, which occurred within a period of 10 days. In addition, it is worth mentioning that reaction (4) implies that Fe^{2+} is continuously released to the solution. Therefore, because olivine is the only supplier of Fe^{2+}, this reaction implicitly indicates that the 'passivating effect' of the coating is less pronounced than under lower temperature conditions, as previously acknowledged by Saldi et al. (2013) and Sissmann et al. (2013). Finally, although reaction (4) is intrinsically responsible for a decrease of the pH, one should keep in mind that in these experiments 1) the pH is mainly buffered by the applied CO_2 pressure; 2) the contribution of reaction (4) to pH is limited by the changes of pH determined by olivine dissolution and magnesite precipitation. As an example, if all the hematite was converted to cronstedtite between day 7 and 19, the corresponding flux of liberated protons would be approximately 4 times lower than that of consumed protons by olivine dissolution (estimated on Si concentrations) over the same time interval. Conversely, assuming that the decrease of Mg concentration is due to the formation of magnesite, the precipitation of this phase would be responsible for a release of H^+ on the same order of magnitude as the H^+ uptake by olivine dissolution. Therefore, both Fe-phyllosilicate

formation at the expense of hematite and magnesite precipitation may have contributed to the resulting apparent decrease in pH observed between day 7 and 19 (see Table 2).

At the end of the third stage of the reaction, the alteration layer was composed of an assemblage of Fe-bearing magnesite and Fe-free amorphous silica coating embedding residual Fe-oxide and possibly Fe-silicate particles (Fig.7). This later evolution of the interfacial layer resulted from the saturation state the fluid attained with respect to the newly-formed phases as a consequence of the physico-chemical transformations that occurred at the olivine/water interface after 'the oxic-to-anoxic' transition. The rapid increase of Fe concentration after 20 days of reaction promoted the formation of (Mg, Fe)-carbonates, which can be considered as the main container of Fe after the attainment of anoxic conditions.

The formation of the final solid assemblage has to be related to the disappearance of the Fe-phyllosilicate during the last stage of the carbonation reaction (19-31 days), because this phase was no longer observed in the interface layer at the end of the experiments Ol-150-1d.

Two non-exclusive hypotheses could explain the removal of the cronstedtite-like phases from the olivine surface. The first resides in the metastable nature of these phases, which would dissolve in favor of the final assemblage as Mg, Si and Fe concentrations increase with the reaction progress (cf. Saldi et al. 2013). Interestingly, several modelling studies indicated that ideal cronstedtite, which may represent the ultimate phase for the observed precursor, is not expected to be stable at T > 100-120 °C, irrespective of the H_2 fugacity and SiO_2 activity (e.g., Zolotov (2014) and references cited therein). However, the actual solubility of cronstedtite has never been experimentally measured at the conditions relevant to our study, so that such possibility has to be considered with caution, taking also into account the large uncertainties

inherent to commonly used thermodynamic databases with respect to complex phyllosilicates (cf. Goddéris et al. 2006; Maher et al. 2009).

Alternatively, we suggest that the Fe-phyllosilicate was stable, and was gradually removed from the surface as it formed consuming the substrate from which it grew (i.e., the Fe–Si-rich interlayer in contact with the olivine surface). This second hypothesis is supported by the observed loss of adhesion of this phase with the olivine surface compared to the previous (hematite+$SiO_{2(am)}$) assemblage. The continuous rocking of the autoclave and the attrition among the mineral grains may have favored the mechanical removal of the Fe-phyllosilicate from the olivine surface, leading to its complete detachment.

To further explore the reliability of these two possible mechanisms, a tentative model of phase equilibria was calculated (Fig. 11), considering cronstedtite as one of the possible saturating phases, in spite of the inherent uncertainties relative to the exact solubility of complex phyllosilicates recalled above. The results illustrate that, depending on the actual oxygen fugacity reached during the course of the experiments, the aqueous solutions of our experiments could be either strongly supersaturated, at saturation or greatly undersaturated with respect to cronstedtite. These calculations support the formation of a cronstedtite-like phase and show that cronstedtite formation is in principle possible under the studied conditions. Whether or not this phase might form from a Fe^{3+}-rich silicate precursor (the identified cronstedtite-like phase) is not known. However, the model also suggests that such a reaction might depend on how the O_2 fugacity varied over the course of the overall reaction: if the drop of $O_{2(aq)}$ activity is large and faster than the rate of cronstedtite formation, this phase might not even appear, leading at the same time to the dissolution of its "potential precursor", the cronstedtite-like phase. The hematite-cronstedtite assemblage is definitely not stable at the conditions where cronstedtite is supposed to form but

452 the formation of one phase at the expense of the other is likely to be controlled by several
453 factors, such as the O_2 fugacity, the solution pH and the amount of SiO_2 adsorbed onto hematite.
454 Comparison between the predicted thermodynamic stability and the occurrence of the above
455 mentioned mineral phases show that the discussed reactions are kinetically controlled by various
456 parameters and may result into the appearance of mineral phases that are metastable with respect
457 to the expected reaction products. As a consequence, the exact fate of these phases remains an
458 open question. However, regardless of the specific mechanism (dissolution or physical
459 detachment), the disappearance of the Fe-phyllosilicate ultimately resulted in the re-exposure of
460 large portions of the olivine surface to dissolution, which is reflected by the observed increase of
461 Fe and Si release rates to solution and the high extent of carbonations recorded after 20 days of
462 reaction.

463 **Reaction sequence in the initially micro-oxic scenario:**

464 In this section, the expected mineralogical evolution during the course of experiment Ol-
465 150-2 is modeled based on the final mineralogical composition of the secondary phases
466 identified after one month of reaction. This work aims at evaluating the extent to which the
467 modeled sequence of secondary minerals could account for the macroscopic observations
468 reported above (e.g., sustained carbonation extent, little to no passivation by any Fe(III)/Si-rich
469 layer and early solubilization of Fe). The thermodynamic model assumes that secondary phases
470 precipitate at equilibrium with the fluid. Moreover, lepidocrocite is not considered because its
471 solubility at high temperature is unknown. The occurrence of lepidocrocite in association with
472 goethite is not uncommon and is most likely favored by slow rates of Fe^{2+} oxidation
473 (Schwertmann and Taylor 1972; Cornell and Schwertmann 2003), which are specific to low-fO_2
474 systems (cf. Morgan and Lahav 2007). However, because the precipitation of lepidocrocite

affects the redox conditions in the same manner as goethite, neglecting its formation does not impact the modeling of the global redox evolution of the system and the estimate of the amount of Fe-oxides formed.

First, the initial $O_{2(aq)}$ concentration needs to be estimated. Because of the slow CH_4 reactivity (cf. Savage et al. 1998; Watanabe et al. 2004; Saldi et al. 2013), it is unlikely that the resulting carbonation rates are representative of the equilibrium between O_2 and methane in the aqueous medium, which would establish very reducing conditions. The observation of ferric oxides and magnetite among the reaction products suggest instead that a non-negligible amount of $O_{2(aq)}$ was present in the system at the beginning of the reaction. The non-stoichiometric nature of the dissolution reaction can be used to estimate the initial $O_{2(aq)}$ concentration in this experiment and provide a reaction pathway model that describes the sequence of the secondary phases we identified at the end of the run. The initial aqueous [Mg]/[Si] ratio was close to the olivine stoichiometry (1.88 vs. 1.76 theoretically), while the initial aqueous [Fe]/[Mg] ratio (0.03) significantly diverged from its theoretical value (0.14). Because the solution was not supersaturated with respect to any Fe(II)-bearing phases, such as siderite, we suggest that the non-stoichiometric [Fe]/[Mg] aqueous ratio can be ascribed to the oxidation of Fe(II) and the subsequent precipitation of insoluble Fe(III)-oxides (i.e., goethite), which therefore sets a lower bound for the initial $O_{2(aq)}$ concentration. The aqueous Fe concentration in the first aliquot being ~5 times lower than expected, our speciation calculations indicate that the initial $O_{2(aq)}$ concentration was at least of 22 μM (i.e., ~10 times lower than in the oxic scenario). This value was selected for the following reaction pathway calculation. The results of these thermodynamic calculations are plotted in Fig. 12. In reasonable agreement with the macroscopic observations, the following features can be seen: (1) the early formation of goethite consuming the dissolved

498 O_2, (2) a spike of $Fe_{(aq)}$ concentration after $O_{2(aq)}$ depletion (goethite is no longer stable); (3) the
499 appearance of magnetite at low extent of dissolution, which forms at the expense of goethite as
500 the conditions become more reducing, and (4) the precipitation of siderite, which represents the
501 analog of ferroan magnesite and whose nucleation is a prerequisite to the growth of magnesite, as
502 shown by the crystal zonations documented by Saldi et al. (2013) and the high extents of
503 carbonation reached in this experiment.

504 It is important to retain that this model does not necessarily describe the mineralogical
505 evolution of the olivine/water interface, because the observed sequence of Fe-oxides was found
506 in mineral aggregates not associated with the olivine surface, while ferroan magnesite mainly
507 appears to be in contact with the olivine grains.

508 The results of the simulation indicate that the mass of goethite produced during the
509 reaction is on the order of 15.4 μmol. If stable, such an amount could cover the olivine surface
510 with a uniform layer of at least 10 nm, which could potentially inhibit the dissolution reaction.
511 However, the comparison with the TEM observations shows the limited coverage of the initial
512 surface by Fe-oxides because they occur as isolated aggregates, and further supports the evidence
513 that little to no inhibition by reaction products occurred during the carbonation reaction.

514 Elementary processes controlling the nature and properties of Fe-Si-rich
515 surface layers

516 As seen above, the concentration levels of dissolved oxygen exert a fundamental role in
517 determining the formation and properties of Fe–Si-rich layers and their control on the fluid
518 chemistry evolution and the extent of the overall reaction. Under oxic conditions, the initial Fe
519 concentration was controlled by the fast precipitation of hematite whereas in the micro-oxic
520 scenario was likely controlled by the slower oxidation rates of Fe^{2+}, which limited the

precipitation of Fe(III)-oxides (goethite and lepidocrocite) as well as their interaction with the olivine surface and their potential clogging ability with respect to any porous Si-rich layer. In the experiment Ol-150-2, because of the low $O_{2(aq)}$ levels, the formation of these Fe(III)-oxides was probably not fast enough to occur in the vicinity of the olivine/water interface but took place in the bulk aqueous solution. This process led to the formation of Fe-oxides aggregates non-associated with the olivine surface such that we could not observe any clear evidence of passivation of the olivine surface. The protecting properties of the Fe–Si-rich surface layers were instead observed in the presence of the (hematite+$SiO_{2(am)}$) assemblage, whose stability was linked to the permanence of oxic conditions (experiments Ol-150-a,b). Overall, TEM observations and modeling of the experimental results show that both the protective coating (hematite+$SiO_{2(am)}$) and the Fe(III)-oxides became unstable when the O_2 in the system was extensively consumed. In facts, the transition to anoxic conditions brought about the formation of a 'cronstedtite-like' phase and magnetite at the expenses of the passivating layer and the Fe(III)-oxides, respectively.

The preferred formation of magnetite vs. the Fe^{3+}-phyllosilicate could result from the fact that, under low $O_{2(aq)}$ concentrations, the saturation with respect to magnetite was reached before equilibrium with respect to the Fe^{3+}-rich phyllosilicate observed to form in the oxic scenario. However, other factors are likely to kinetically control the formation of either phase. In particular the hematite-amorphous silica association seems to constitute an ideal precursor for the formation of the Fe^{3+}-rich phyllosilicate, whereas the transformation of hematite into magnetite might be inhibited by the presence of chemically adsorbed Si (Carlson and Schwertmann 1981; Doelsch et al. 2000; Pokrovski et al. 2003). This is also in agreement with the evidence that

543 increasing SiO_2 activities generally favor the formation of Fe-rich serpentine minerals instead of
544 magnetite (Frost and Beard 2007; Evans 2008).

545 These considerations show how the different mechanisms and rates of formation of Fe-
546 oxides between oxic and micro-oxic to anoxic conditions result in a significantly different impact
547 on the reactivity of the olivine surface, by favoring or not the formation of protective Fe−Si-rich
548 surface layers. As reported by previous studies, coatings of Fe(III)-free $SiO_{2(am)}$ are typically
549 non-passivating (Daval et al. 2009, 2010; King et al. 2011; Saldi et al. 2013), and, as such, they
550 likely did not hinder the formation of the secondary ferroan magnesite crystals observed to
551 precipitate on top of the $SiO_{2(am)}$-layer the during the late stage of the carbonation reaction.
552

553 ## IMPLICATIONS

554 The described trends of fast dissolution rate / dramatic slowdown / resumption may
555 represent a general pathway in coupled dissolution-precipitation processes (e.g., Frugier et al.
556 2008; Michelin et al. 2013). The sensitivity of geochemical systems to redox conditions, as
557 demonstrated by the nature of the secondary phases, raises new key criteria for the optimization
558 of the carbonation process of ultramafic rocks. Our results indicate, for example, that extent and
559 location of the carbonation process might be controlled by adjusting the flow of injection of fresh
560 oxygenated fluids, because desirable O_2 levels can be achieved as a function of the dissolution
561 rates of Fe-bearing silicates, such as olivine, and the mineral surface available for the reaction in
562 the reservoir. We further suggest that, at an industrial scale, the impact of other gases co-injected
563 together with CO_2 should be considered in greater details (cf. Knauss et al. 2005), as some of
564 them have the potential to buffer the redox system and ultimately control the rate of olivine
565 carbonation.

Acknowledgements

This work was supported by the Director, Office of Science, Office of Basic Energy Sciences, Chemical Sciences, Geosciences, and Biosciences Division, of the U.S. Department of Energy under Contract No. DE-AC02-05CH11231. The authors thank Tracy Mattox for the technical assistance during ICP-OES analyses at LBNL and Timothy Teague for helping us with sample preparation and for the technical support provided at SEM on UC campus. Martiane Cabié (CP2M, Marseille, France) is warmly thanked for her help with the preparation of FIB thin sections. STXM-based XAS data were acquired at beamline10ID-1 at the CLS, which is supported by the NSERC, the CIHR, the NRC, and the University of Saskatchewan. Special thanks go to Jian Wang and Jay Dynes for their expert support of the STXM at the CLS. This manuscript benefited from the most helpful comments of an anonymous reviewer. We thank Dionysis Foustoukos for his additional comments and the editorial assistance.

REFERENCES CITED

Andreani, M., Luquot, L., Gouze, P., Godard, M., Hoise, E., and Gibert, B. (2009) Experimental study of carbon sequestration reactions controlled by the percolation of CO_2-rich brine through peridotites. Environmental Science and Technology, 43, 1226–1231.

Andreani, M., Muñoz, M., Marcaillou, C., and Delacour, A. (2013). μXANES study of iron redox state in serpentine during oceanic serpentinization. Lithos, 178(C), 70–83.

Barnes, C.S. (2006) ThermoSolver: an integrated educational thermodynamics software program. H.B. Thesis Abstract, 46 p.

Barnes, C.S., and Koretsky, M.D. (2004) in Engineering and Chemical Thermodynamics. John Wiley and Sons, 553 p.

Béarat, H., McKelvy, M., Chizmeshya, A., Gormley, D., Nunez, R., Carpenter, R., Squires, K., and Wolf, G. (2006) Carbon sequestration via aqueous olivine mineral carbonation: role of

passivating layer formation Environmental Science and Technology, 40, 4802–4808.

Bourdelle, F., Benzerara, K., Beyssac, O., Cosmidis, J., Neuville, D.R., Brown, G.E., and Paineau, E. (2013) Quantification of the ferric/ferrous iron ratio in silicates by scanning transmission X-ray microscopy at the Fe $L_{2,3}$ edges. Contributions to Mineralogy and Petrology, 166, 423–434.

Carlson, L., and Schwertmann, U. (1981) Natural ferrihydrites in surface deposits from Finland and their association with silica. Geochimica et Cosmochimica Acta, 45, 421–429.

Casey, W., Westrich, H., Banfield, J., Ferruzzi, G., and Arnold, G. (1993) Leaching and reconstruction at the surfaces of dissolving chain-silicate minerals. Nature, 366, 253–255

Cornell, R.M., and Schwertmann, U. (2003) The Iron Oxides: Structures, properties, reactions, occurrences and uses. Second edition. Wiley-VCH GmbH & Co. KGaA, 664 p.

Daval, D., Sissmann, O., Menguy, N., Saldi, G.D., Guyot, F., Martinez, I., Corvisier, J., Garcia, B., Machouk, I., Knauss, K.G., and Hellmann, R. (2011) Influence of amorphous silica layer formation on the dissolution rate of olivine at 90 °C and elevated pCO_2. Chemical Geology, 284, 193-209.

Daval, D., Hellmann, R., Saldi, G.D., Wirth, R. and Knauss, K.G. (2013) Linking nm-scale measurements of the anisotropy of silicate surface reactivity to macroscopic dissolution rate laws: New insights based on diopside. Geochimica et Cosmochimica Acta, 107, 121–134.

Daval, D., Martinez, I., Guigner, J.-M., Hellmann, R., Corvisier, J., Findling, N., Dominici C., Goffé, B., and Guyot, F. (2009) Mechanism of wollastonite carbonation deduced from micro to nanometer length scale observations. American Mineralogist 94, 1707–1726.

Daval, D., Testemale, D., Recham, N., Tarascon, J.-M., Siebert, J., Martinez, I., Guyot, F. (2010) Fayalite (Fe_2SiO_4) dissolution kinetics determined by X-ray absorption spectroscopy. Chemical Geology, 275, 161–175.

Davis, C.C., Chen, H.-W., and Edwards, M. (2002). Modeling Silica Sorption to Iron Hydroxide. Environmental Science And Technology 36, 582–587.

Davis, M.C., Brouwer, W.J., Wesolowski, D.J., Anovitz, L.M., Lipton, A.S., and Mueller, K.T. (2009) Magnesium silicate dissolution investigated by ^{29}Si MAS, ^{1}H–^{29}Si CPMAS, ^{25}Mg QCPMG, and ^{1}H–^{25}Mg CP QCPMG NMR. Physical Chemistry Chemical Physics, 11, 7013–7021.

Doelsch, E., Rose, J., Masion, A., Bottero, J.Y., Nahon, D., and Bertsch, P.M. (2000) Speciation

and Crystal Chemistry of Iron(III) Chloride Hydrolyzed in the Presence of SiO 4Ligands. 1. An Fe K-Edge EXAFS Study. Langmuir, 16, 4726–4731.

Drobne, D., Milani, M., Leser, V., and Tatti, F. (2007) Surface damage induced by FIB milling and imaging of biological samples is controllable. Microscopy Research and Technique, 70 (10), 895–903.

Dufaud, F., Martinez, I., and Shilobreeva, S. (2009) Experimental study of Mg-rich silicates carbonation at 400 and 500 °C and 1kbar. Chemical Geology, 265, 79–87.

Dzombak, D.A., and Morel, F.M.M. (1990) Surface Complexation Modeling: Hydrous Ferric Oxide. Wiley-Interscience eds., 416 p..

Evans, B. (2008). Control of the Products of Serpentinization by the Fe2+ Mg− 1 Exchange Potential of Olivine and Orthopyroxene. Journal of Petrology, 49 (10), 1873–1887.

Frost, B.R., and Beard, J.S. (2007). On Silica Activity and Serpentinization. Journal of Petrology, 48 (7), 1351–1368.

Frugier, P., Gin, S., Minet, Y., Chave, T., Bonin, B., Godon, N., Lartigue, J.E., Jollivet, P., Ayral, A., De Windt, L., and Santarini, G. (2008) SON68 nuclear glass dissolution kinetics: Current state of knowledge and basis of the new GRAAL model. Journal of Nuclear Materials, 380, 8–21.

Garcia, B., Beaumont, V., Perfetti, E., and Rouchon, V. (2010) Experiments and geochemical modelling of CO2 sequestration by olivine: Potential, quantification. Applied Geochemistry, 25, 1383–1396.

Geiger, C.A., Henry, D.L., Bailey, S.W., and Maj, J.J. (1983) Crystal structure of cronstedtite-2H2. Clays and Clay Minerals, 31, 97–108.

Gerdemann, S., O'Connor, W., Dahlin, D., Penner, L., and Rush, H. (2007) Ex situ aqueous mineral carbonation. Environmental Science and Technology, 41, 2587–2593.

Giammar, D., Bruant, R., and Peters, C.A. (2005) Forsterite dissolution and magnesite precipitation at conditions relevant for deep saline aquifer storage and sequestration of carbon dioxide. Chemical Geology, 217, 257–276.

Goddéris, Y., François, L.M., Probst, A., Schott, J., Moncoulon, D., Labat, D., and Viville, D. (2006) Modelling weathering processes at the catchment scale: The WITCH numerical model. Geochimica et Cosmochimica Acta, 70, 1128–1147.

Guyot, F., Daval, D., Dupraz, S., Martinez, I., Menez, B., and Sissmann, O. (2011) CO_2

geological storage: the environmental mineralogy perspective. Comptes Rendus Geoscience, 343, 246-259.

Hellmann, R., Wirth, R., Daval, D., Barnes, J.-P., Penisson, J.-M., Tisserand, D., Epicier T., Florin, B., and Hervig, R.L. (2012) Unifying natural and laboratory chemical weathering with interfacial dissolution–reprecipitation: A study based on the nanometer-scale chemistry of fluid–silicate interfaces. Chemical Geology, 294-295, 203–216.

Hu, M., Ji, R.-P., and Jiang J.-S. (2010) Materials Research Bulletin. Materials, 45, 1811–1815.

Hybler, J., Petříček, V., Ďurovič, S., and Smrčok, L. (2000) Refinement of the crystal structure of cronstedtite-1T. Clays and Clay Minerals, 48, 331–338

Iler, R.K. (1979) The chemistry of silica: solubility, polymerization, colloid and surface and surface properties, and biochemistry. John Wiley and Sons, 867 p.

Jeon, B.-H., Dempsey, B.A., and Burgos, W.D. (2003) Kinetics and Mechanisms for Reactions of Fe(II) with Iron(III) Oxides. Environmental Science and Technology, 37, 3309–3315.

Johnson, N.C., Thomas, B., Maher, K., Rosenbauer, R.J., Bird, D., and Brown, G.E.Jr. (2014) Olivine dissolution and carbonation under conditions relevant for in situ carbon storage Chemical Geology, 373, 93–105.

Jones, A.M., Collins, R.N., Rose, J., and Waite, T.D. (2009) The effect of silica and natural organic matter on the Fe(II)-catalysed transformation and reactivity of Fe(III) minerals. Geochimica et Cosmochimica Acta, 73, 4409–4422.

Kaznatcheev, K.V., Karunakaran, C., Lanke, U.D., Urquhart, S.G., Obst, M., Hitchcock, A.P. (2007) Soft X-ray spectromicroscopy beamline at the CLS: commissioning results. Nuclear Instruments and Methods in Physics Research A, 582, 96–99.

King, H.E., Plümper, O., and Putnis, A. (2010) Effect of secondary phase formation on the carbonation of olivine. Environmental Science And Technology, 44, 6503–6509.

King, H.E., Plümper, O., Geisler, T., and Putnis, A. (2011) Experimental investigations into the silicification of olivine: implications for the reaction mechanism and acid neutralization. American Mineralogist, 96, 1503–1511.

Knauss, K.G., and Copenhaver, S.A. (1995) The solubility of p-xylene in water as a function of temperature and pressure and calculated thermodynamic quantities. Geochimica et Cosmochimica Acta, 59, 2443–2448.

Knauss, K., Johnson, J., and Steefel, C. (2005) Evaluation of the impact of CO_2, co-contaminant

gas, aqueous fluid and reservoir rock interactions on the geologic sequestration of CO_2. Chemical Geology, 217(3-4), 339–350.

Langford, R.M. (2006) Focused Ion Beams techniques for nanomaterials characterization. Microscopy Research and Technique, 69(7), 538–549.

Le Guillou, C., Changela, H., and Brearley, A.J. (2015) Widespread oxidized and hydrated amorphous silicates in CR chondrites matrices: implications for alteration conditions and H2 degassing of asteroids. Earth and Planetary Science Letters, 420, 162–173.

Maher, K., Steefel, C.I., White, A.F., and Stonestrom, D.A. (2009) The role of reaction affinity and secondary minerals in regulating chemical weathering rates at the Santa Cruz Soil Chronosequence, California. Geochimica et Cosmochimica Acta, 73, 2804–2831.

Mayer, J., Giannuzzi, L.A., Kamino, T., and Michael, J. (2007) TEM sample preparation and FIB-induced damage. MRS Bulletin, 32, 400–407.

Michelin, A., Burger, E., Rebiscoul, D., Neff, D., Bruguier, F., Drouet, E., Dillmann, P., and Gin, S. (2013) Silicate Glass Alteration Enhanced by Iron: Origin and Long-Term Implications. Environmental Science and Technology, 47, 750–756.

Morgan, B., and Lahav, O. (2007) The effect of pH on the kinetics of spontaneous Fe(II) oxidation by O_2 in aqueous solution – basic principles and a simple heuristic description. Chemosphere, 68, 2080–2084.

Oelkers, E.H. (2001) An experimental study of forsterite dissolution rates as a function of temperature and aqueous Mg and Si concentrations. Chemical Geology, 175, 485–494.

Oelkers, E.H., Gíslason, S.R., and Matter, J. (2008) Mineral Carbonation of CO_2. Elements, 4, 333–337.

Olsson, J., Bovet, N., Makovicky, E., Bechgaard, K., Balogh, Z. and Stipp, S.L.S. (2012) Olivine reactivity with CO2 and H2O on a microscale: Implications for carbon sequestration. Geochimica et Cosmochimica Acta, 77, 86–97.

Parkhurst, D.L., and Appelo, C.A.J. (1999) User's guide to PHREEQC (version 2) – a computer program for speciation, batch-reaction, one-dimensional transport, and inverse geochemical calculations. US Geological Survey Water-resources Investigation Report 99-4259. 312 p.

Pedersen, H.D., Postma, D., Jakobsen, R., and Larsen, O. (2005) Fast transformation of iron oxyhydroxides by the catalytic action of aqueous Fe(II). Geochimica et Cosmochimica Acta, 69, 3967–3977.

716 Pokrovski, G. S., Schott, J., Farges, F., and Hazemann, J.-L. (2003) Iron (III)-silica interactions
717 in aqueous solution: Insights from X-ray absorption fine structure spectroscopy. Geochimica
718 et Cosmochimica Acta 67, 3559–3573.
719 Qafoku, O., Kovarik, L., Kukkadapu, R.K., Ilton, E.S., Arey, B.W., Tucek, J., Felmy, A.R.
720 (2012) Fayalite dissolution and siderite formation in water-saturated supercritical CO_2.
721 Chemical Geology, 332-333, 124–135.
722 Ravel, B., and Newville, M (2005). ATHENA, ARTEMIS, HEPHAESTUS: data analysis for X-
723 ray absorption spectroscopy using IFEFFIT. Journal of Synchrotron Radiation, 12(4), 537–
724 541.
725 Rubanov, S., and Munroe, P.R. (2004) FIB-induced damage in silicon. Journal of Microscopy,
726 214(3), 213–221.
727 Rusch, B., Hanna, K., and Humbert, B. (2010). Coating of quartz silica with iron oxides:
728 Characterization and surface reactivity of iron coating phases. Colloids and Surfaces A:
729 Physicochemical and Engineering Aspects, 353, 172–180.
730 Saldi, G.D., Daval, D., Morvan, G., and Knauss, K.G. (2013) The role of Fe and redox
731 conditions in olivine carbonation rates: An experimental study of the rate limiting reactions
732 at 90 and 150 °C in open and closed systems. Geochimica et Cosmochimica Acta, 118, 157–
733 183.
734 Savage, P.E., Yu, J., Stylski, N., and Brock, E.E. (1998) Kinetics of methane oxidation in
735 supercritical water. Journal of Supercritical Fluids, 12, 141–153.
736 Schott, J., and Berner, R. (1983) X-ray photoelectron studies of the mechanism of iron silicate
737 dissolution during weathering. Geochimica et Cosmochimica Acta, 47, 2233–2240.
738 Schott, J., Pokrovsky, O.S., and Oelkers, E.H. (2009). The link between mineral dissolution/
739 precipitation kinetics and solution chemistry. Reviews in Mineralogy and Geochemistry, 70,
740 207–258.
741 Schott, J., Pokrovsky, O.S., Spalla, O., Devreux, F., Gloter, A., and Mielczarski, J.A. (2012)
742 Formation, growth and transformation of leached layers during silicate minerals dissolution:
743 The example of wollastonite. Geochimica et Cosmochimica Acta, 98, 259–281.
744 Schwertmann, U., and Taylor, R.M. (1972) The transformation of lepidocrocite to goethite.
745 Clays and Clay Minerals, 20, 151–158.
746 Seyfried, W.Jr., Gordon, P., and Dickson, F. (1979) New reaction cell for hydrothermal solution

747 equipment. American Mineralogist, 64, 646–649.
748 Sissmann, O., Daval, D., Brunet, F., Guyot, F., Verlaguet, A., Pinquier, Y., Findling, N., and
749 Martinez, I. (2013) The deleterious effects of secondary phases on olivine carbonation yield:
750 Insight from time-resolved aqueous-fluid sampling and FIB-TEM characterization.
751 Chemical Geology, 357, 186–202.
752 Smith, A.J., Munroe, P.R., Tran, T., and Wainwright, M.S. (2001) FIB preparation of a sensitive
753 porous catalyst for TEM elemental mapping at high magnifications. Journal of Materials
754 Science, 36(14), 3519–3524.
755 Smrčok, L., Ďurovič, S., Petříček, V., and Weiss, Z. (1994) Refinement of the crystal structure of
756 cronstedtite-3T. Clays and Clay Minerals, 42, 554–551.
757 Thompson, L.E., Rice, P.M., Delenia, E., Lee, V.Y., Brock, P.J., Magbitang, T.P., Dubois, G.,
758 Volksen, W., Miller, R.D., and Kim, H-C. (2006) Imaging thin films of nanoporous low-k
759 dielectrics: comparison between ultramicrotomy and focused ion beam preparations for
760 transmission electron microscopy. Microscopy and Microanalysis, 12, 156–159.
761 Velbel, M.A. (1993) Formation of protective surface layers during silicate-mineral weathering
762 under well-leached, oxidizing conditions. American Mineralogist, 78, 405–414.
763 Wang, F., and Giammar, D.E. (2012) Forsterite dissolution in saline water at elevated
764 temperature and high CO_2 pressure. Environmental Science And Technology, 47, 168–173.
765 Watanabe, M., Sato, T., Inomata, H., Smith, R.L.Jr., Arai, K., Kruse, A., and Dinjus, E. (2004)
766 Chemical Reactions of C_1 compounds in near-critical and supercritical water. Chemical
767 Reviews, 104, 5803–5821.
768 White, A.F., and Brantley, S.L. (2003) The effect of time on weathering of silicate minerals: why
769 do weathering rates differ in the laboratory and field? Chemical Geology, 202, 479–506.
770 Williams, A.G.B., and Scherer, M.M. (2004) Spectroscopic Evidence for Fe(II)−Fe(III) Electron
771 Transfer at the Iron Oxide−Water Interface. Environmental Science and Technology, 38,
772 4782–4790.
773 Zolotov, M.Y. (2014) Formation of brucite and cronstedtite-bearing mineral assemblages on
774 Ceres. Icarus, 228, 13–26.
775

776 **Table 1.** Summary of the experimental conditions of the batch experiments conducted in this study at 150
777 °C and at a CO_2 partial pressures of 100 bar using the San Carlos olivine. SA stands for the
778 initial BET surface area of olivine. The CO_2 fugacity (fCO_2) was calculated using the software
779 ThermoSolver 1.0 (Barnes and Koretsky, 2004). Run Ol-150-1d is the experiment Ol-150 of
780 Saldi et al. (2013) renamed.
781

Run #	**Powder mass** [g]	**Starting volume** [ml]	**SA/water** [cm^2/ml]	fCO_2 [bar]	**Duration** [days]
Oxic conditions					
Ol-150-1a	1.998	178.0	1.7	85	6.9
Ol-150-1b	1.992	179.5	1.7	85	17.1
Ol-150-1c	1.998	180.0	1.7	85	19.0
Ol-150-1d	1.987	171.8	1.7	85	31.0
Micro-oxic conditions					
Ol-150-2	2.011	177.4	1.7	85	31.9

782

Table 2. Summary of the results obtained from the series of batch experiment (Ol-150-1a to d) performed at T=150 °C and pCO_2 =100 bar on SC olivine within an aqueous medium initially equilibrated with the atmosphere. Aqueous fluid composition, recalculated pH (pH_c , see text) and the saturation states of the fluid (Ω=IAP/K_{sp}) with respect to magnesite [Ω(Mgs)] and amorphous silica [$\Omega(SiO_{2(am)})$] are reported. Note that 'IAP' designates the ion activity product for the species of interest in the calculation of the saturation state.

Run # Ol-150-1a. 7days

Sample	elapsed time [days]	pH_m (25°C)	pH_c (150°C)	Mg [mM]	Si [mM]	Fe [μM]	Mg/Si	Ω(Mgs)	$\Omega(SiO_{2(am)})$
Ol-150-1a-1	0	4.98	4.03	0.85	0.46	< DL	1.85	0.02	0.04
Ol-150-1a-2	0.9	5.90	4.81	6.59	3.48	< DL	1.89	3.30	0.33
Ol-150-1a-3	2.6	5.95	4.90	8.57	4.53	< DL	1.89	5.82	0.42
Ol-150-1a-4	3.7	6.00	4.91	9.20	4.89	< DL	1.88	6.45	0.46
Ol-150-1a-5	4.7	6.01	4.93	9.67	5.12	< DL	1.89	7.28	0.48
Ol-150-1a-6	5.7	6.02	4.95	10.13	5.39	< DL	1.88	7.77	0.50
Ol-150-1a-7	6.6	6.01	4.95	10.36	5.66	< DL	1.83	8.08	0.53
Ol-150-1a-8	6.9	6.02	4.95	10.11	6.42	< DL	1.57	8.02	0.53

Run # Ol-150-1b. 17days

Sample	elapsed time [days]	pH_m (25°C)	pH_c (150°C)	Mg [mM]	Si [mM]	Fe [μM]	Mg/Si	Ω(Mgs)	$\Omega(SiO_{2(am)})$
Ol-150-1b-1	0.1	5.26	4.19	1.30	0.73	< DL	1.80	0.06	0.07
Ol-150-1b-2	0.7	5.58	4.76	5.93	3.23	< DL	1.84	2.53	0.30
Ol-150-1b-3	1.8	5.96	4.85	7.50	4.07	< DL	1.84	4.30	0.38
Ol-150-1b-4	4.0	6.05	4.90	8.73	4.74	< DL	1.84	6.05	0.44
Ol-150-1b-5	6.7	6.08	4.94	9.52	5.17	< DL	1.84	7.34	0.48
Ol-150-1b-6	8.8	6.03	4.93	9.27	5.80	< DL	1.60	6.92	0.54
Ol-150-1b-7	11.0	5.96	4.88	8.10	6.30	< DL	1.29	5.12	0.59
Ol-150-1b-8	14.0	5.93	4.83	7.12	6.76	< DL	1.05	3.83	0.63
Ol-150-1b-9	16.0	5.94	4.81	6.76	7.08	< DL	0.96	3.41	0.66
Ol-150-1b-10	17.1	5.91	4.80	6.60	7.21	< DL	0.92	3.23	0.67

< DL = below the detection limit; nd = not determined.

Run # Ol-150-1c. 19 days

Sample	elapsed time [days]	pH_m (25°C)	pH_c (150°C)	Mg [mM]	Si [mM]	Fe [µM]	Mg/Si	Ω(Mgs)	$\Omega(SiO_{2(am)})$
Ol-150-1c-1	0.0	5.21	4.09	1.00	0.53	< DL	1.87	0.03	0.05
Ol-150-1c-2	0.6	5.89	4.76	5.85	3.18	< DL	1.84	2.44	0.30
Ol-150-1c-3	1.7	6.03	4.87	7.89	4.26	< DL	1.85	4.83	0.40
Ol-150-1c-4	3.9	6.11	4.92	9.09	4.97	< DL	1.83	6.62	0.47
Ol-150-1c-5	6.8	6.19	4.96	10.11	5.71	< DL	1.77	8.38	0.53
Ol-150-1c-6	9.7	6.07	4.92	9.04	6.28	< DL	1.44	6.54	0.59
Ol-150-1c-7	11.9	6.04	4.88	8.05	6.73	< DL	1.20	5.05	0.63
Ol-150-1c-8	15.0	5.96	4.84	7.21	7.29	< DL	0.99	3.94	0.68
Ol-150-1c-9	17.0	5.93	4.82	6.91	7.52	< DL	0.92	3.58	0.70
Ol-150-1c-10	18.0	5.97	4.81	6.71	7.58	< DL	0.88	3.35	0.71
Ol-150-1c-11	19.0	5.88	4.81	6.70	7.97	< DL	0.84	3.34	0.75

Run # Ol-150-1d. 31days

Sample	elapsed time [days]	pH_m (25°C)	pH_c (150°C)	Mg [mM]	Si [mM]	Fe [µM]	Mg/Si	Ω(Mgs)	$\Omega(SiO_{2(am)})$
Ol-150-1d-1	0.1	5.13	4.07	0.94	0.54	< DL	1.76	0.03	0.05
Ol-150-1d-2	0.3	5.70	4.62	4.04	2.27	< DL	1.78	1.03	0.21
Ol-150-1d-3	0.9	5.90	4.81	6.73	3.59	< DL	1.88	3.38	0.34
Ol-150-1d-4	1.3	5.92	4.85	7.50	4.04	< DL	1.85	4.31	0.38
Ol-150-1d-5	3.9	6.03	4.92	9.03	4.95	< DL	1.82	6.54	0.46
Ol-150-1d-6	4.9	6.06	4.93	9.23	5.03	< DL	1.83	6.86	0.47
Ol-150-1d-7	6.2	6.08	4.94	9.59	5.13	< DL	1.87	7.47	0.48
Ol-150-1d-8	8.2	5.99	4.96	10.06	5.52	< DL	1.82	8.30	0.52
Ol-150-1d-9	10.9	6.09	4.93	9.42	6.09	< DL	1.55	7.19	0.57
Ol-150-1d-10	14.9	5.89	4.85	7.60	6.88	< DL	1.10	4.44	0.64
Ol-150-1d-11	20.3	5.89	4.81	6.64	10.71	11.55	0.62	3.28	1.00
Ol-150-1d-12	24.2	5.85	4.75	5.69	14.17	7.68	0.40	2.30	1.33
Ol-150-1d-13	29.0	5.99	4.73	5.34	14.52	5.93	0.37	1.98	1.36
Ol-150-1d-14	31.0	nd	4.72	5.22	12.74	7.76	0.41	1.88	1.19

792 < DL = below the detection limit; nd = not determined.

Table 3. Summary of the results obtained from the batch experiment conducted at T=150 °C and pCO_2 =100 bar on SC olivine. under initially anoxic conditions (run # Ol-150-2). In addition to saturation states of the fluid (Ω=IAP/K_{sp}) with respect to magnesite [Ω(Mgs)**]** and amorphous silica [$\Omega(SiO_{2(am)})$], the table includes the values of the saturation ratio of the fluid with respect to siderite [Ω(Sid)]. Note that 'IAP' designates the ion activity product for the species of interest in the calculation of the saturation state.

Sample	**elapsed time** [days]	**pH** (25°C)	**pH** (150°C)	**Mg** [mM]	**Si** [mM]	**Fe** [µM]	**Mg/Si**	**Fe/Si**	**Ω(Mgs)**	**Ω(Sid)**	**Ω($SiO_{2(am)}$)**
Ol-150-2-1	0.0	5.30	4.03	0.83	0.44	25.20	1.88	5.7E-02	0.02	0.03	0.04
Ol-150-2-2	0.6	5.87	4.75	5.72	3.59	9.02	1.59	2.5E-03	2.33	0.11	0.34
Ol-150-2-3	1.0	6.01	4.83	7.16	5.71	5.70	1.25	1.0E-03	3.88	0.08	0.53
Ol-150-2-4	1.9	5.98	4.82	6.97	10.43	3.40	0.67	3.3E-04	3.66	0.05	0.98
Ol-150-2-5	2.9	5.92	4.82	6.93	14.84	2.77	0.47	1.9E-04	3.61	0.04	1.39
Ol-150-2-6	4.7	5.91	4.78	6.27	15.78	3.30	0.40	2.1E-04	2.87	0.04	1.48
Ol-150-2-7	6.6	5.88	4.78	6.17	15.07	5.28	0.41	3.5E-04	2.77	0.07	1.41
Ol-150-2-8	8.6	5.91	4.78	6.18	14.84	4.56	0.42	3.1E-04	2.78	0.06	1.39
Ol-150-2-9	11.6	5.86	4.77	6.00	14.69	4.89	0.41	3.3E-04	2.60	0.06	1.37
Ol-150-2-10	15.0	5.87	4.76	5.82	14.30	4.87	0.41	3.4E-04	2.42	0.06	1.34
Ol-150-2-11	20.0	5.82	4.74	5.50	13.97	4.88	0.39	3.5E-04	2.13	0.06	1.31
Ol-150-2-12	23.0	5.82	4.73	5.38	13.97	5.39	0.39	3.9E-04	2.02	0.06	1.31
Ol-150-2-13	28.0	5.85	4.71	5.17	13.50	5.88	0.38	4.4E-04	1.84	0.06	1.26
Ol-150-2-14	31.9	5.81	4.70	5.05	13.55	5.39	0.37	4.0E-04	1.74	0.06	1.27

List of Figures

Figure 1. Evolution of Mg, Si and Fe concentrations as a function of time during the experiments Ol-150-1a-d, conducted at T=150 °C and pCO_2=100 bar, under initially oxic conditions. Each of these runs is a replicate of the same experimental conditions but stopped at different reaction times: a) 7days; b) 17 days; c) 19 days; d) 31 days. The dashed lines drawn on the plots correspond to the saturation condition with respect to magnesite (Mgs) and amorphous silica ($SiO_{2(am)}$). The calculated magnesite saturation condition is attained at pH=4.6.

Figure 2. Changes of Mg, Si and Fe concentrations during the batch olivine carbonation experiment conducted at T=150 °C and pCO_2=100 bar, under initially micro-oxic conditions. The dashed lines drawn on the plot correspond to the saturation conditions (SI=0) with respect to magnesite (Mgs) and amorphous silica ($SiO_{2(am)}$). The calculated magnesite saturation condition is attained at pH=4.6.

Figure 3. SEM microphotographs of olivine grain surfaces after the carbonation experiments conducted under initially oxic conditions (expt. Ol-150-1a-d) at T=150 °C and pCO_2=100bar. (a) olivine grain covered by a Fe−Si-rich altered layer after 7 days of reaction (Ol-150-1a); (b) olivine grain reacted for a duration of 17 days and largely covered by the Fe−Si-rich coating (Ol-150-1b); c) detail of dissolution etch pits at 19 days of reaction showing the granular structure of the Fe−Si-rich coating (Ol-150-1c); d) carbonated olivine grain presenting a thick layer of magnesite aggregates above an amorphous silica-rich interlayer (Ol-150-1d; see also Saldi et al., 2013). Note the presence of a small magnesite crystal in contact with the olivine grain surface in (b).

Figure 4. TEM analyses of a FIB-foil extracted from an olivine grain reacted for 7 days at T=150 °C and pCO_2= 100 bar. a) TEM image showing the appearance of the FIB-foil cut across a 10 μm wide etch pit; the thickness of the Fe−Si-rich coating is not uniform but correlated with the morphology of the reacted surface. b) Close-up view of the area highlighted in the right corner of

(a), showing a detail of the Fe-Si-rich coating with the corresponding SAED pattern indicating that the Fe-rich phase observed after 7 days of reaction is hematite. c) Detail of the sharp olivine/ Fe−Si-rich coating highlighted in (a), showing the porous structure of the hematite needle-like aggregates. d) Enlarged view of the contact between olivine and the alteration layer indicated by the corresponding box in (a): the Fe-Si-rich altered layer is thinner than in the other sectors but is denser and exhibits a finer texture. Single spot EDX spectra 1 and 2 from the corresponding regions in (c) and (d) indicate the close association between hematite and amorphous silica.

Figure 5. TEM analyses of the FIB foil obtained from an olivine grain reacted for 17 days at T=150 °C and pCO_2= 100 bar. a) TEM image showing the appearance of the interfacial Fe−Si-rich layer, primarily composed of a Fe-phyllosilicate and a thin inner layer consisting of a $SiO_{2(am)}$+Fe-oxide assemblage. The EDX spectra relative to the Fe-phyllosilicate (1), the inner layer (2) and the unreacted olivine (3) are provided. The peak at 8 keV on the spectra corresponds to the copper of the TEM grid. b) SAED pattern of the interfacial Fe-phyllosilicate with the results of indexing and the corresponding lattice planes of the identified phase: cronstedtite. c) The particles of the neo-formed Fe-silicate locally consist of individual aggregates displaying a concentric onion-like structure. d) Example of HRTEM image used for the measurements of the inter-reticular distances of the studied Fe-phyllosilicate.

Figure 6. Determination of the Fe(II)/Fe(III) relative proportion in the Fe−Si-rich coating at 17 days of reaction by analysis of the XANES spectra obtained with scanning transmission X-ray spectroscopy (STXM). The quantification of the $Fe^{3+}/\Sigma Fe$ ratio was accomplished by measuring the area ratios of the L_2 and L_3 peaks of the XANES spectra (see text for details). a) Image of one of the two FIB-sections studied with a detail of the analyzed Fe−Si-rich coating highlighted in yellow color; b) example of two XANES spectra representative of the unreacted olivine (blue) and the Fe-phyllosilicate formed after 17 days (green), which is assimilated to a cronstedtite precursor. The two vertical dotted lines represent the L_3-edge energies fixed to quantify the Fe^{3+} concentration (cf. Bourdelle et al., 2013).

Figure 7. TEM images of the FIB foil extracted from a carbonated olivine grain after 31 days of reaction at T=150 °C and pCO_2= 100 bar and under initially oxic conditions. a) FIB section showing a Mg-carbonate assemblage covering an olivine grain with the interposition of the evolved Fe−Si-rich layer. b) Detail of the olivine-carbonate interface showing the occurrence of an essentially Fe-free amorphous silica layer (see EDX spectrum and corresponding SAED pattern at the margin of the picture) containing sparsely disseminated residual hematite and/or Fe-silicate crystals.

Figure 8. SEM images of carbonation products after the reaction initiated under micro-oxic conditions (expt. Ol-150-2). a) Example of extensively dissolved/carbonated olivine crystals; b) detail of an olivine carbonated grain with EDX spectrum showing the presence of Fe in the precipitated magnesite.

Figure 9. Example of a Fe-oxide aggregate of particles of different generation formed during the experiment started at low O_2 fugacity (Ol-150-2). These masses of Fe-oxides are primarily composed of goethite, another Fe-oxide phase, identified as lepidocrocite, and magnetite crystals exhibiting their typical octahedral habit (see also Fig.10). These aggregates are not found in association with olivine grain surfaces.

Figure 10. TEM image of a Fe-oxide aggregate showing a sequence of three different generations of particles with different size and morphology, along with the corresponding SAED patterns and an EDX spectrum. The indexing of the SAED patterns here shown allowed to determine the identity of the smaller particles in the bottom part of the picture (goethite) and the big particle on top of the aggregate (magnetite), whereas the elongated particles in between were identified as lepidocrocite crystals.

Figure 11. Activity diagram for the system FeO-SiO_2-H_2O-CO_2 at the CO_2 fugacity of our experiments. Here are reported the solubility curves for magnetite (Mag), cronstedtite (Cdt), siderite (Sd), greenalite (Gre), minnesotaite (or Fe-talc) (Mns) and $SiO_{2(am)}$, together with the

888 datapoints corresponding to the samples of the experiments Ol-150-1d and Ol-150-2 where we
889 could measure Fe in solution. The black solubility lines of magnetite and cronstedtite are relative
890 to an $O_{2(aq)}$ activity of $10^{-5.6}$, which is 100 times lower than the fluid initially equilibrated with the
891 atmosphere. This value was chosen as representative of the transition towards anoxic conditions,
892 where the observed Fe-phyllosilicate might start to form. Two additional cronstedtite solubility
893 lines (blue dashed lines) are reported for increased anoxic conditions ($a(O_{2(aq)})=10^{-25}$ and 10^{-35}),
894 which may have been reached during the course of the experiments, as revealed by the
895 thermodynamic simulations reported in Saldi et al. (2013). This plot illustrates that the fluids of
896 our experiments can be strongly supersaturated, at saturation or greatly undersaturated with
897 respect to cronstedtite, depending on the assumed O_2 fugacity for the system.

898

899 **Figure 12.** Thermodynamic model describing the fate of Fe during the experiment conducted
900 under micro-oxic conditions. The simulation was conducted with PHREEQC assuming that the
901 initial $O_{2(aq)}$ concentration was fixed by the equilibrium with goethite for the Fe concentration
902 measured at the beginning of the experiment. Fe(II) and O_2 concentrations and the mass of Fe-
903 phases precipitated are plotted as a function of the dissolved amount of SC-olivine on the left and
904 right y-axis, respectively. Because of the low $O_{2(aq)}$ content, the mineralogical changes involving
905 goethite, magnetite and siderite occur in the early stage of the reaction and do not affect
906 appreciably the olivine dissolution.

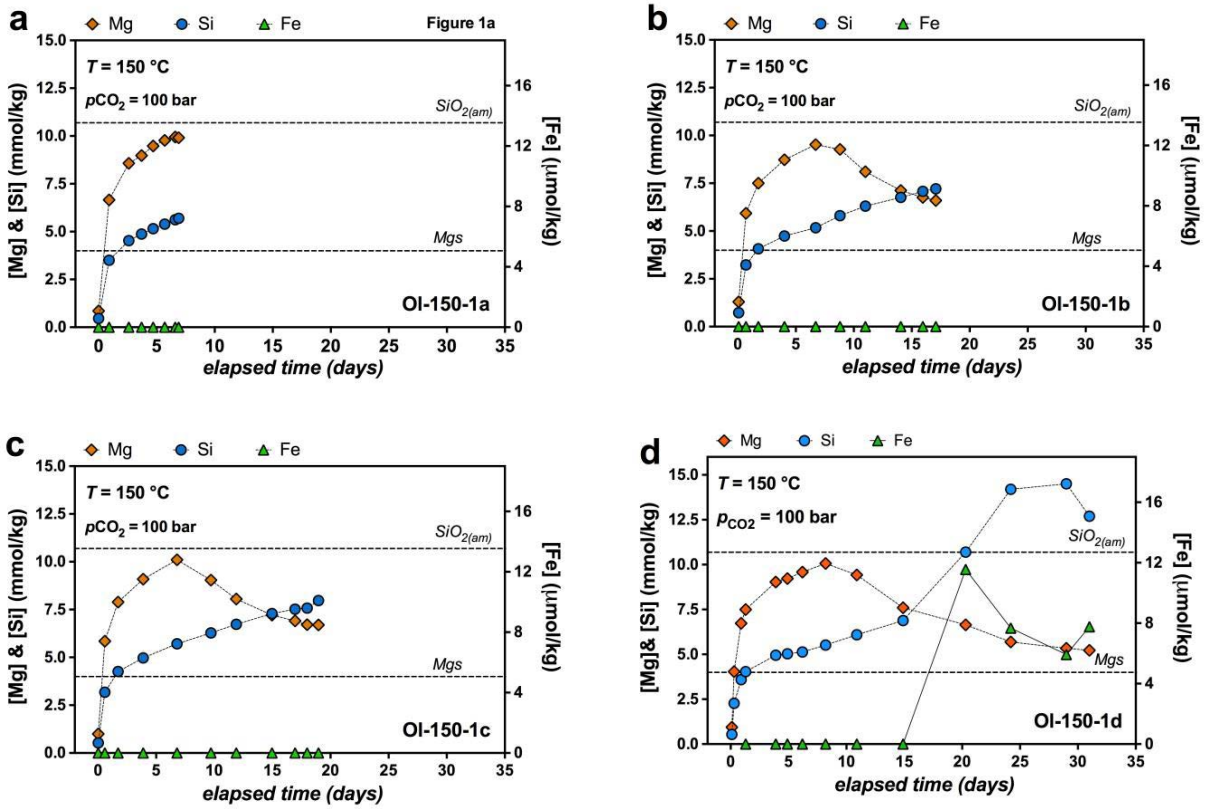

Figure 1. Evolution of Mg, Si and Fe concentrations as a function of time during the experiments Ol-150-1a-d, conducted at T=150 °C and pCO$_2$=100 bar, under initially oxic conditions. Each of these runs is a replicate of the same experimental conditions but stopped at different reaction times: a) 7days; b) 17 days; c) 19 days; d) 31 days. The dashed lines drawn on the plots correspond to the saturation condition with respect to magnesite (Mgs) and amorphous silica ($SiO_{2(am)}$). The calculated magnesite saturation condition is attained at pH=4.6.

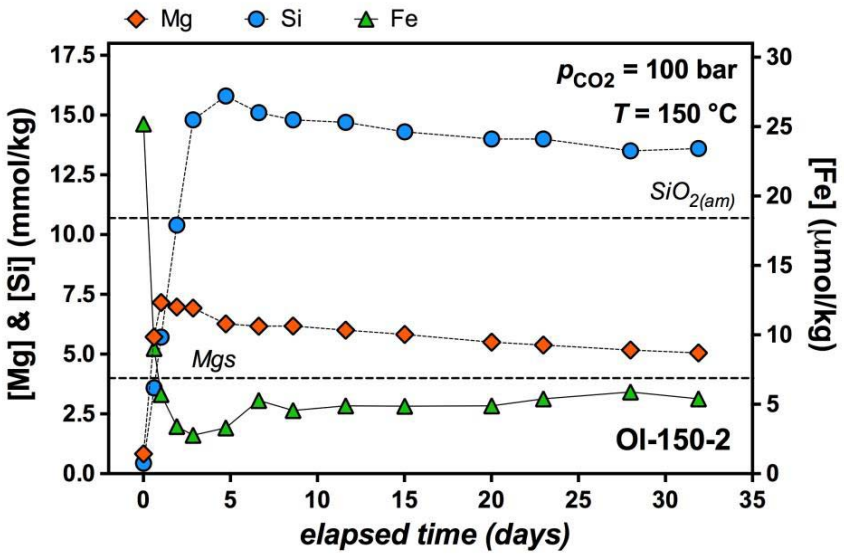

Figure 2. Changes of Mg, Si and Fe concentrations during the batch olivine carbonation experiment conducted at T=150 °C and pCO$_2$=100 bar, under initially micro-oxic conditions. The dashed lines drawn on the plot correspond to the saturation conditions (SI=0) with respect to magnesite (Mgs) and amorphous silica ($SiO_{2(am)}$). The calculated magnesite saturation condition is attained at pH=4.6.

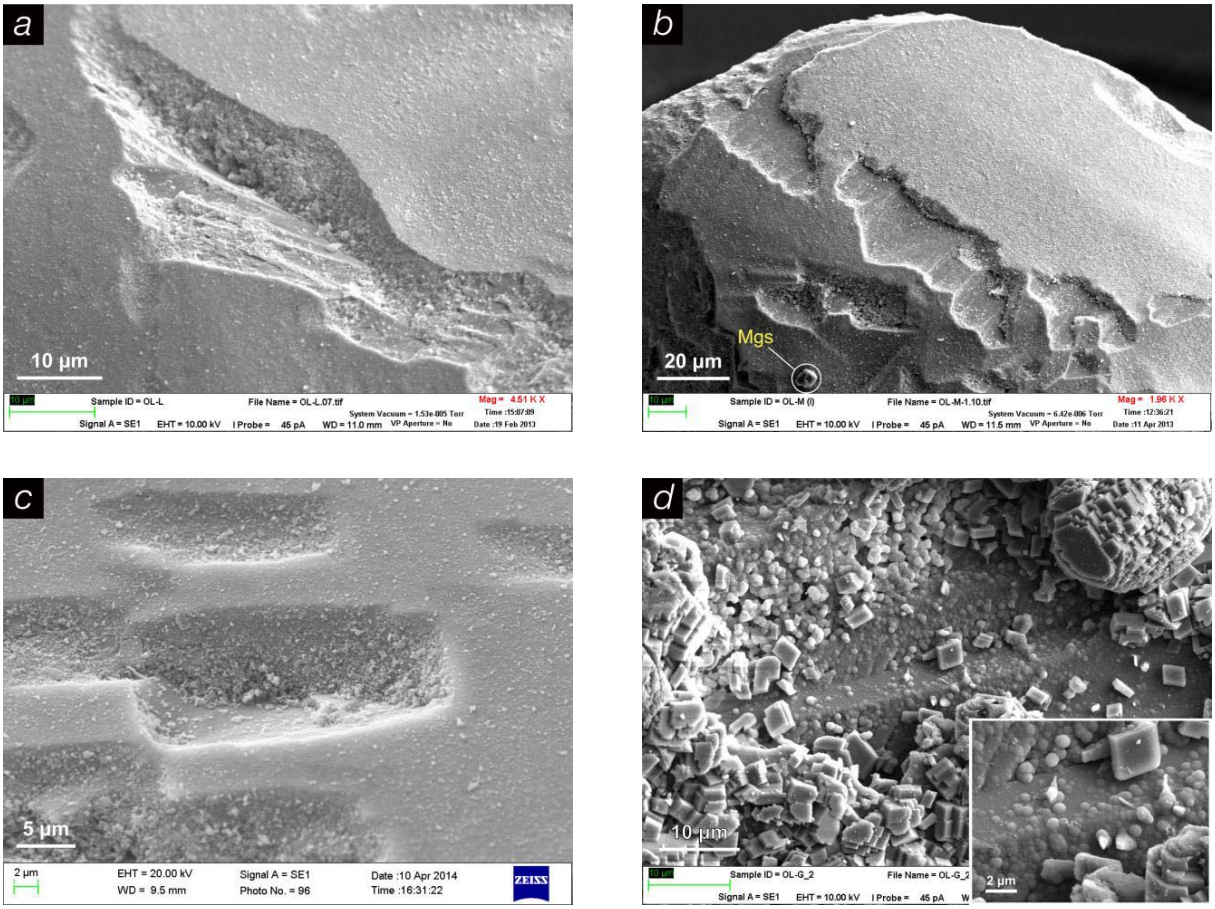

Figure 3. SEM microphotographs of olivine grain surfaces after the carbonation experiments conducted under initially oxic conditions (expt. Ol-150-1a-d) at T=150 °C and pCO_2=100bar. (a) olivine grain covered by a Fe−Si-rich altered layer after 7 days of reaction (Ol-150-1a); (b) olivine grain reacted for a duration of 17 days and largely covered by the Fe−Si-rich coating (Ol-150-1b); c) detail of dissolution etch pits at 19 days of reaction showing the granular structure of the Fe−Si-rich coating (Ol-150-1c); d) carbonated olivine grain presenting a thick layer of magnesite aggregates above an amorphous silica-rich interlayer (Ol-150-1d; see also Saldi et al., 2013). Note the presence of a small magnesite crystal in contact with the olivine grain surface in (b).

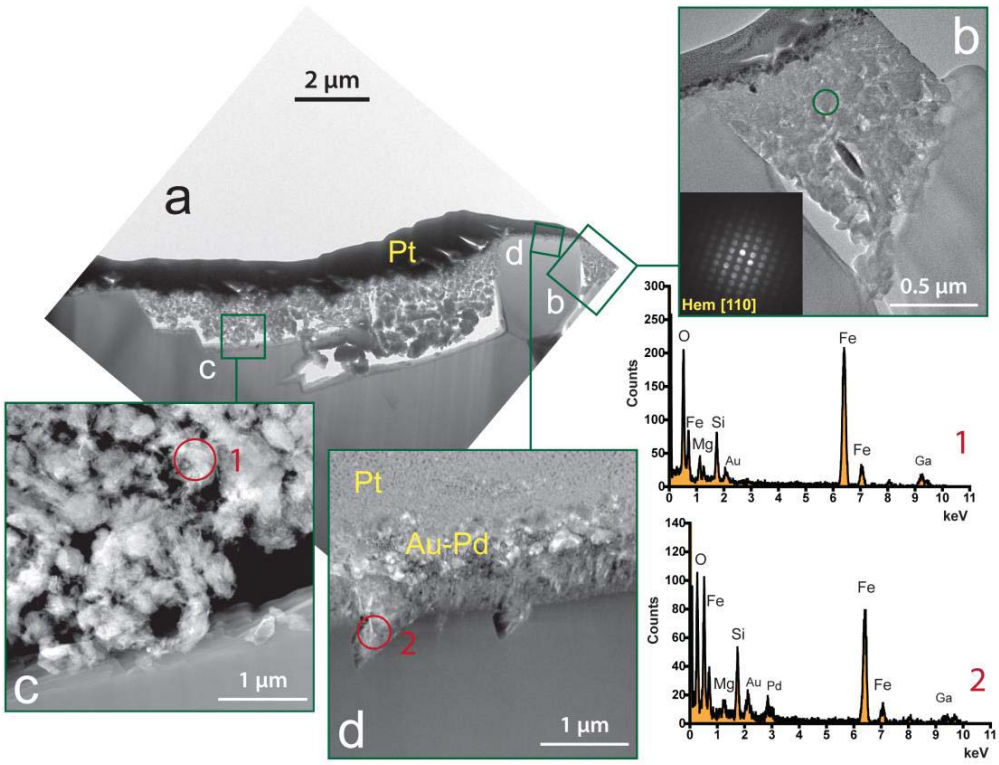

Figure 4. TEM analyses of a FIB-foil extracted from an olivine grain reacted for 7 days at T=150 °C and pCO_2= 100 bar. a) TEM image showing the appearance of the FIB-foil cut across a 10 µm wide etch pit; the thickness of the Fe–Si-rich coating is not uniform but correlated with the morphology of the reacted surface. b) Close-up view of the area highlighted in the right corner of (a), showing a detail of the Fe-Si-rich coating with the corresponding SAED pattern indicating that the Fe-rich phase observed after 7 days of reaction is hematite. c) Detail of the sharp olivine/ Fe–Si-rich coating highlighted in (a), showing the porous structure of the hematite needle-like aggregates. d) Enlarged view of the contact between olivine and the alteration layer indicated by the corresponding box in (a): the Fe-Si-rich altered layer is thinner than in the other sectors but is denser and exhibits a finer texture. Single spot EDX spectra 1 and 2 from the corresponding regions in (c) and (d) indicate the close association between hematite and amorphous silica.

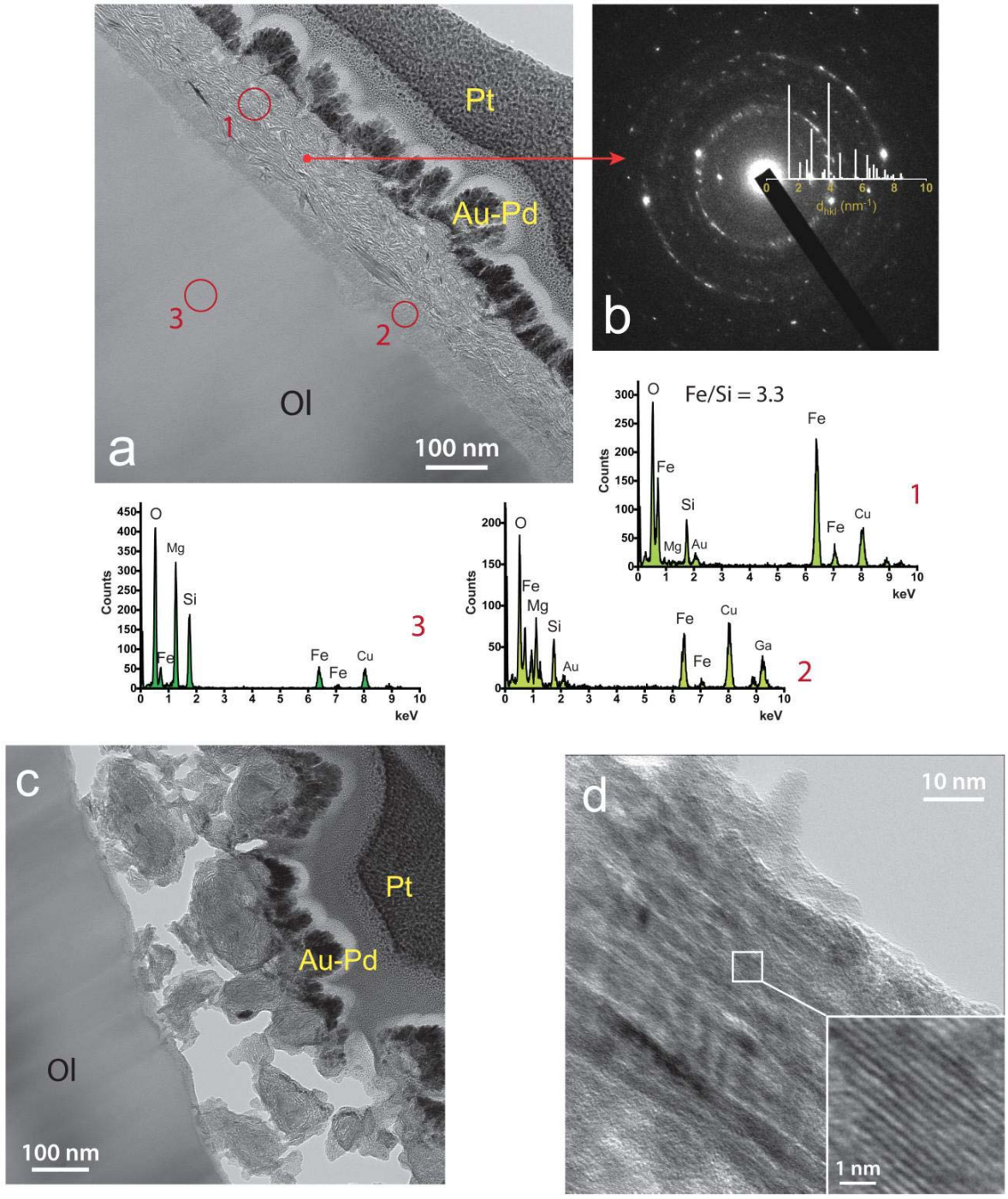

Figure 5. TEM analyses of the FIB foil obtained from an olivine grain reacted for 17 days at T=150 °C and pCO_2= 100 bar. a) TEM image showing the appearance of the interfacial Fe−Si-rich layer, primarily composed of a Fe-phyllosilicate and a thin inner layer consisting of a $SiO_{2(am)}$+Fe-oxide assemblage. The EDX spectra relative to the Fe-phyllosilicate (1), the inner layer (2) and the unreacted olivine (3) are provided. The peak at 8 keV on the spectra corresponds to the copper of the TEM grid. b) SAED pattern of the interfacial Fe-phyllosilicate with the results of indexing and the corresponding lattice planes of the identified phase: cronstedtite. c) The particles of the neo-formed Fe-silicate locally consist of individual aggregates displaying a concentric onion-like structure. d) Example of HRTEM image used for the measurements of the inter-reticular distances of the studied Fe-phyllosilicate.

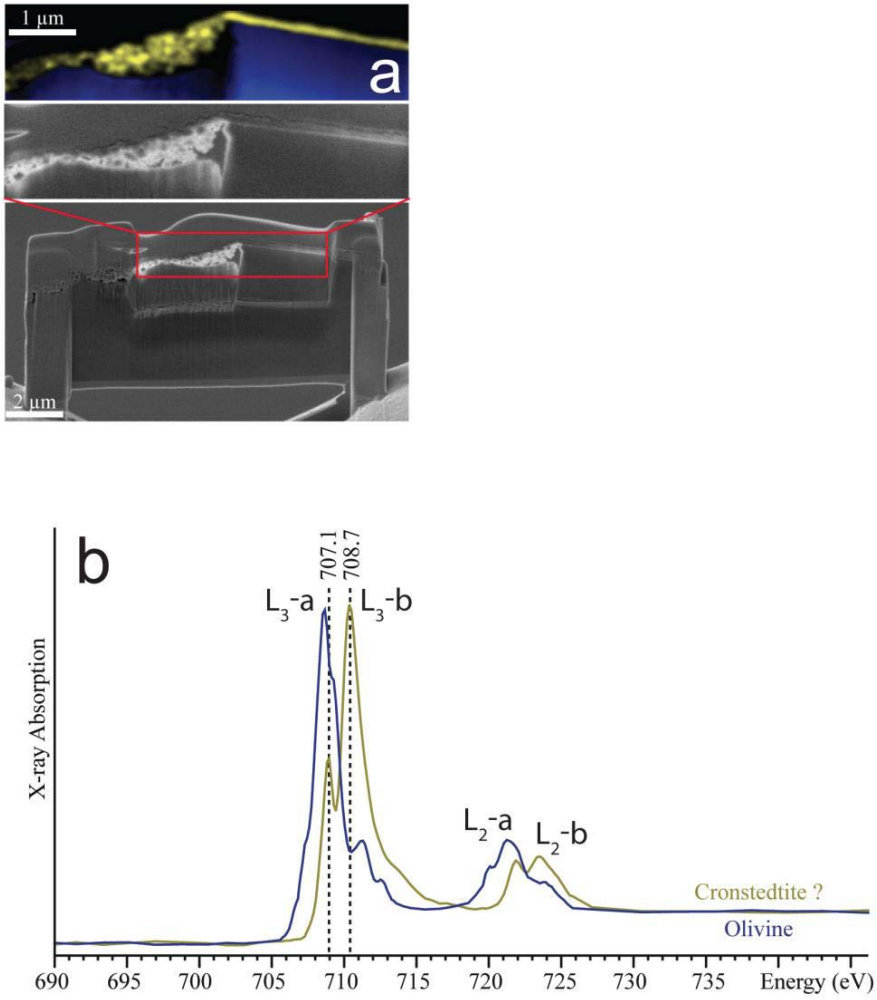

Figure 6. Determination of the Fe(II)/Fe(III) relative proportion in the Fe−Si-rich coating at 17 days of reaction by analysis of the XANES spectra obtained with scanning transmission X-ray spectroscopy (STXM). The quantification of the $Fe^{3+}/\Sigma Fe$ ratio was accomplished by measuring the area ratios of the L_2 and L_3 peaks of the XANES spectra (see text for details). a) Image of one of the two FIB-sections studied with a detail of the analyzed Fe−Si-rich coating highlighted in yellow color; b) example of two XANES spectra representative of the unreacted olivine (blue) and the Fe-phyllosilicate formed after 17 days (green), which is assimilated to a cronstedtite precursor. The two vertical dotted lines represent the L_3-edge energies fixed to quantify the Fe^{3+} concentration (cf. Bourdelle et al., 2013).

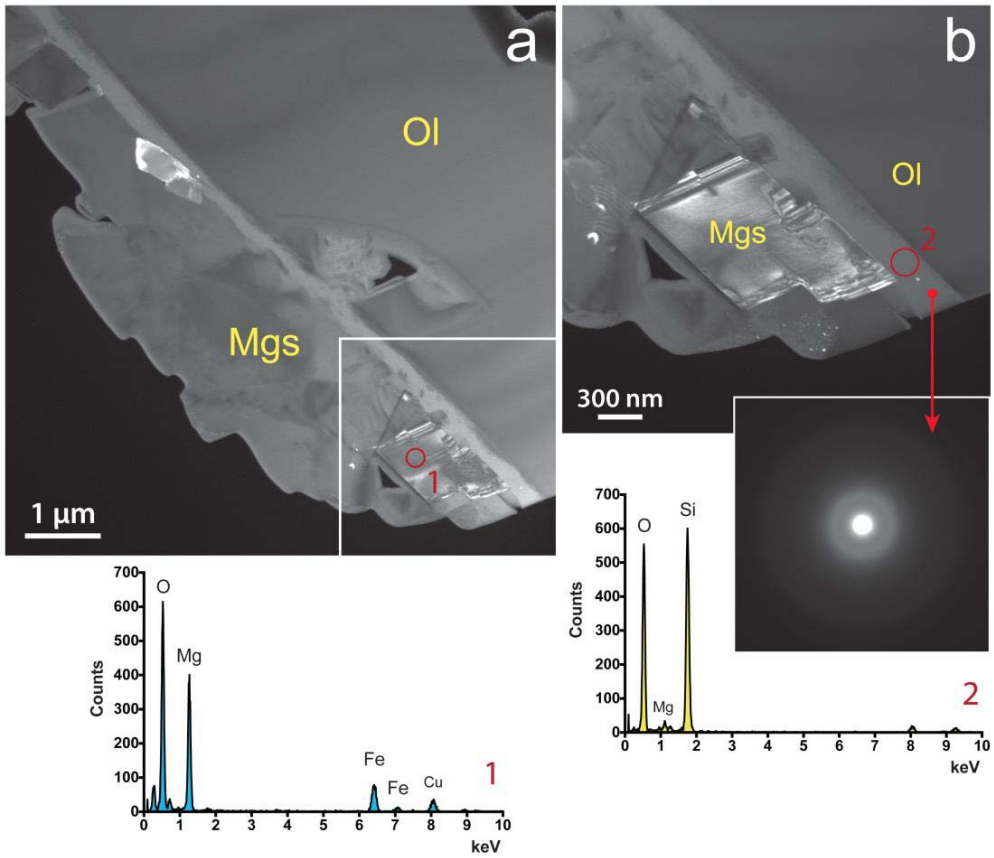

Figure 7. TEM images of the FIB foil extracted from a carbonated olivine grain after 31 days of reaction at T=150 °C and pCO_2= 100 bar and under initially oxic conditions. a) FIB section showing a Mg-carbonate assemblage covering an olivine grain with the interposition of the evolved Fe−Si-rich layer. b) Detail of the olivine-carbonate interface showing the occurrence of an essentially Fe-free amorphous silica layer (see EDX spectrum and corresponding SAED pattern at the margin of the picture) containing sparsely disseminated residual hematite and/or Fe-silicate crystals.

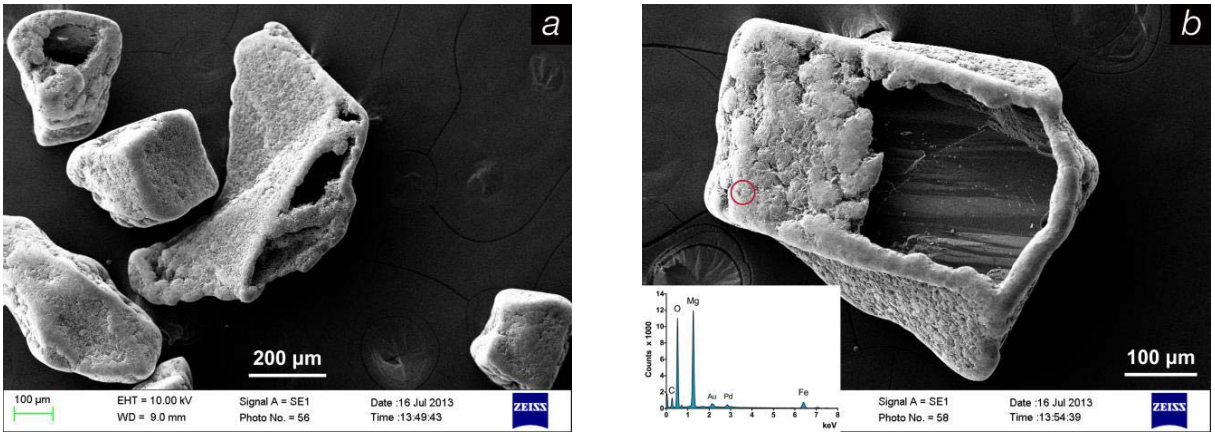

Figure 8. SEM images of carbonation products after the reaction initiated under micro-oxic conditions (expt. Ol-150-2). a) Example of extensively dissolved/carbonated olivine crystals; b) detail of an olivine carbonated grain with EDX spectrum showing the presence of Fe in the precipitated magnesite.

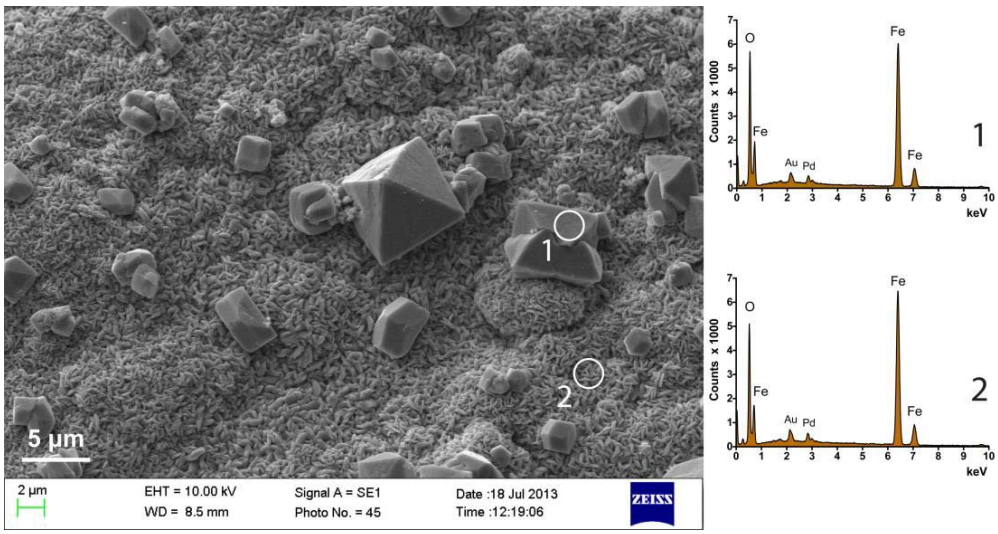

Figure 9. Example of a Fe-oxide aggregate of particles of different generation formed during the experiment started at low O_2 fugacity (Ol-150-2). These masses of Fe-oxides are primarily composed of goethite, another Fe-oxide phase, identified as lepidocrocite, and magnetite crystals exhibiting their typical octahedral habit (see also Fig.10). These aggregates are not found in association with olivine grain surfaces.

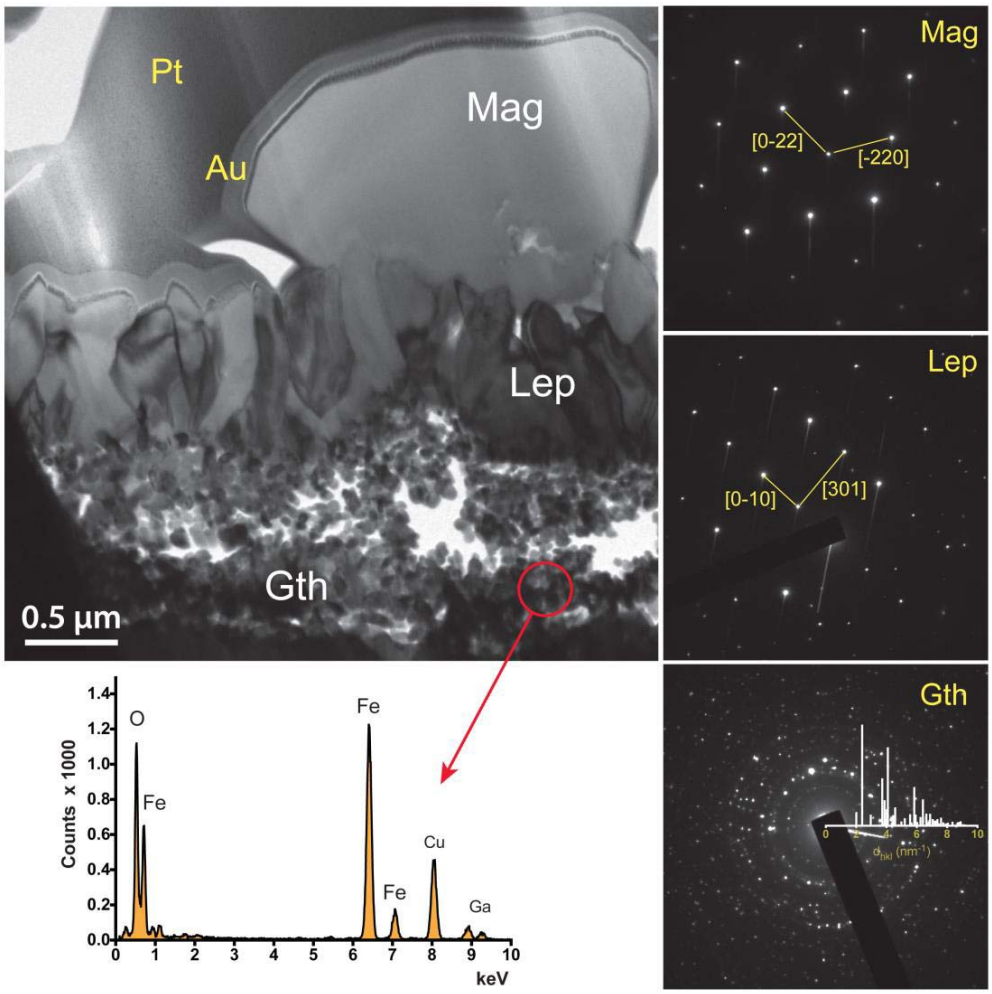

Figure 10. TEM image of a Fe-oxide aggregate showing a sequence of three different generations of particles with different size and morphology, along with the corresponding SAED patterns and an EDX spectrum. The indexing of the SAED patterns here shown allowed to determine the identity of the smaller particles in the bottom part of the picture (goethite) and the big particle on top of the aggregate (magnetite), whereas the elongated particles in between were identified as lepidocrocite crystals.

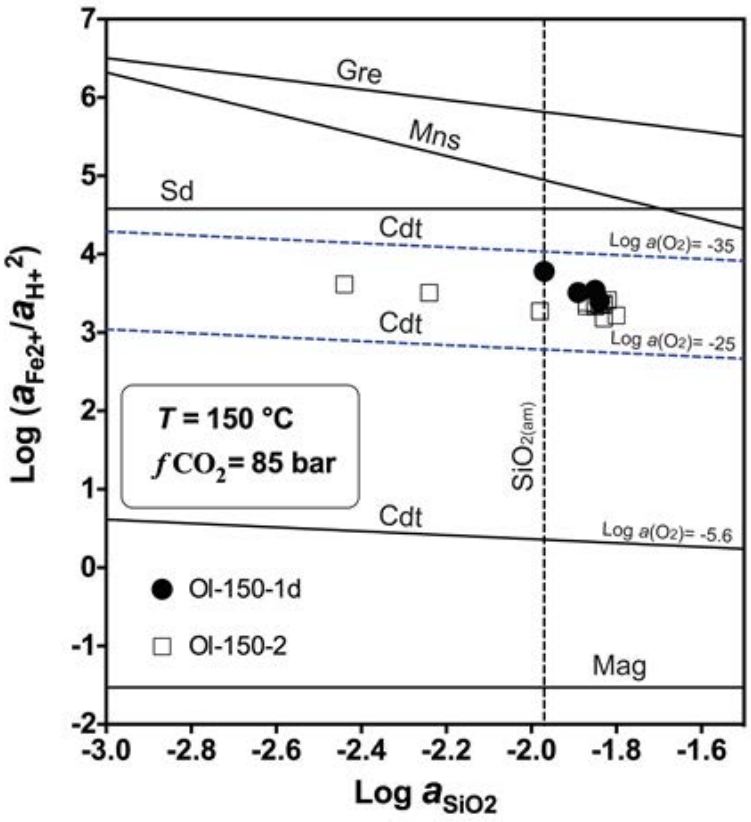

Figure 11. Activity diagram for the system FeO-SiO_2-H_2O-CO_2 at the CO_2 fugacity of our experiments. Here are reported the solubility curves for magnetite (Mag), cronstedtite (Cdt), siderite (Sd), greenalite (Gre), minnesotaite (or Fe-talc) (Mns) and $SiO_{2(am)}$, together with the datapoints corresponding to the samples of the experiments Ol-150-1d and Ol-150-2 where we could measure Fe in solution. The black solubility lines of magnetite and cronstedtite are relative to an $O_{2(aq)}$ activity of $10^{-5.6}$, which is 100 times lower than the fluid initially equilibrated with the atmosphere. This value was chosen as representative of the transition towards anoxic conditions, where the observed Fe-phyllosilicate might start to form. Two additional cronstedtite solubility lines (blue dashed lines) are reported for increased anoxic conditions ($a(O_{2(aq)})=10^{-25}$ and 10^{-35}), which may have been reached during the course of the experiments, as revealed by the thermodynamic simulations reported in Saldi et al. (2013). This plot illustrates that the fluids of our experiments can be strongly supersaturated, at saturation or greatly undersaturated with respect to cronstedtite, depending on the assumed O_2 fugacity for the system.

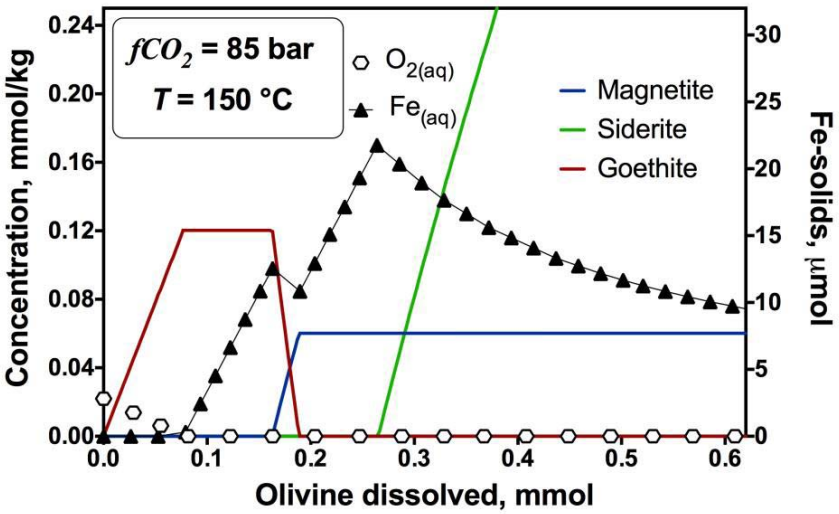

Figure 12. Thermodynamic model describing the fate of Fe during the experiment conducted under micro-oxic conditions. The simulation was conducted with PHREEQC assuming that the initial $O_{2(aq)}$ concentration was fixed by the equilibrium with goethite for the Fe concentration measured at the beginning of the experiment. Fe(II) and O_2 concentrations and the mass of Fe-phases precipitated are plotted as a function of the dissolved amount of SC-olivine on the left and right y-axis, respectively. Because of the low $O_{2(aq)}$ content, the mineralogical changes involving goethite, magnetite and siderite occur in the early stage of the reaction and do not affect appreciably the olivine dissolution.